

2019-08-23

# Rupture geometries in anisotropic amphibolite recorded by pseudotachylytes in the Gairloch Shear Zone, NW Scotland

Campbell, LR

<http://hdl.handle.net/10026.1/14770>

---

10.1144/sjg2019-003

Scottish Journal of Geology

Geological Society

---

*All content in PEARL is protected by copyright law. Author manuscripts are made available in accordance with publisher policies. Please cite only the published version using the details provided on the item record or document. In the absence of an open licence (e.g. Creative Commons), permissions for further reuse of content should be sought from the publisher or author.*

1 **Rupture geometries in anisotropic amphibolite recorded by pseudotachylytes in the Gairloch**  
2 **Shear Zone, NW Scotland**

3 Lucy R. Campbell<sup>1,2\*</sup>, Richard J. Phillips<sup>1</sup>, Rachel C. Walcott<sup>3</sup> & Geoffrey E. Lloyd<sup>1</sup>

4 <sup>1</sup>School of Earth and Environment, University of Leeds, LS2 9JT, UK

5 <sup>2</sup>Present address: School of Geography, Earth and Environmental Sciences, Plymouth University, PL4  
6 8AA, UK.

7 <sup>3</sup> National Museums Scotland, Chambers Street. Edinburgh, EH1 1JF, UK

8 \*Corresponding author (email: [lucy.campbell@plymouth.ac.uk](mailto:lucy.campbell@plymouth.ac.uk))

9

10 **Abstract**

11 Recent earthquakes involving complex multi-fault rupture have increased our appreciation of the  
12 variety of rupture geometries and fault interactions that occur within the short duration of coseismic  
13 slip. Geometrical complexities are intrinsically linked with spatially heterogeneous slip and stress  
14 drop distributions, and hence need incorporating into seismic hazard analysis. Studies of exhumed  
15 ancient fault zones facilitate investigation of rupture processes in the context of lithology and  
16 structure at seismogenic depths. In the Gairloch Shear Zone, NW Scotland, foliated amphibolites  
17 host pseudotachylytes that record rupture geometries of ancient low-magnitude ( $\leq M_w$  3) seismicity.  
18 Pseudotachylyte faults are commonly foliation parallel, indicating exploitation of foliation planes as  
19 weak interfaces for seismic rupture. Discordance and complexity are introduced by fault  
20 segmentation, stepovers, branching and brecciated dilational volumes. Pseudotachylyte geometries  
21 indicate that slip nucleation initiated simultaneously across several parallel foliation planes with  
22 millimetre and centimetre separations, leading to progressive interaction and ultimately linkage of  
23 adjacent segments and branches within a single earthquake. Interacting with this structural control,  
24 a lithological influence of abundant low disequilibrium melting-point amphibole facilitated coseismic  
25 melting, with relatively high coseismic melt pressure encouraging transient dilational sites. These  
26 faults elucidate controls and processes that may upscale to large active fault zones hosting major  
27 earthquake activity.

28 Supplementary material: Supplementary Figures 1 and 2, unannotated versions of field photographs  
29 displayed in Figures 4a and 5 respectively, are available at

30

31

32 Seismic hazard mapping depends heavily on understanding the geometry of fault planes and  
33 earthquake rupture, which are best understood from examination of surface ruptures and analogous  
34 exhumed fault zones. Recent earthquakes have widened understanding of the possible complexities  
35 of rupture, allowing the creation of many alternative models to a simple single planar fault, for  
36 example the multi-segment 2016  $M_w$  7.8 Kaikōura earthquake (Hamling *et al.* 2017), the 2018  $M_w$   
37 7.9 offshore Kodiak earthquake (Ruppert *et al.* 2018) and the 2010  $M_w$  7.2 El-Mayor-Cucapah  
38 earthquake (Fletcher *et al.* 2016). The potential for multi-segment rupture is, however, not typically  
39 accounted for in seismic hazard modelling (Nissen *et al.* 2016). Supporting this new understanding is  
40 a body of research characterising the geometry and development of exhumed fault zones, which  
41 reveal greater complexity at scales typically less than the resolution of seismological records (e.g.  
42 Sibson 1975, Swanson, 1988, Allen *et al.*, 2002, Di Toro & Pennacchioni 2005, Rowe *et al.*, 2018).  
43 Significantly, exhumed faults reveal geometries and deformation mechanisms of faults at  
44 seismogenic depths (e.g. Sibson 1975; Swanson 1988; Allen *et al.* 2002; Di Toro and Pennacchioni  
45 2005; Ujiie *et al.* 2007; Griffith *et al.* 2010; Rowe *et al.* 2011, 2018; Kirkpatrick *et al.* 2012; Ferrand *et*  
46 *al.* 2018).

47 Pseudotachylyte, a melt-derived fault rock produced during coseismic frictional heating (Sibson  
48 1975), remains one of the best recognised markers of ancient seismicity (Cowan 1999; Rowe &  
49 Griffith 2015). It has been extensively utilised to study seismic source parameters and rupture  
50 geometries from exhumed fault zones worldwide and across a range of depths (e.g. Sibson 1975;  
51 Swanson 1988; Allen *et al.* 2002; Di Toro and Pennacchioni 2005; Ujiie *et al.* 2007; Griffith *et al.*  
52 2010; Rowe *et al.* 2011, 2018; Kirkpatrick *et al.* 2012; Ferrand *et al.* 2018). Pseudotachylyte-bearing  
53 faults illustrate a variety of fault plane and damage zone geometries, including the melt-generating  
54 fault planes, tensile off-fault injection veins, chaotic networks of off-fault veining, and dilational sites  
55 often hosting breccias, all of which may illustrate the heterogeneous and dynamic environment of  
56 coseismic rupture (Sibson 1975, 1985; Swanson 2005; Kirkpatrick & Shipton 2009; Ngo *et al.* 2012;  
57 Griffith & Prakash 2015; Rowe *et al.* 2018).

58 In the context of successive frictional failure, pseudotachylytes are frequently inferred to weld fault  
59 planes once they have cooled, such that later brittle slip events rarely reactivate unaltered  
60 pseudotachylyte-bearing faults (Mitchell *et al.* 2016, Phillips *et al.*, 2019). Consequentially, a suite of  
61 pseudotachylyte faults may preserve snapshots of seismic rupture evolution that have evaded  
62 reactivation and/or destruction by later slip events along the same fault plane, although they may be  
63 subject to subsequent recrystallization, viscous deformation and mineralogical alteration (Kirkpatrick  
64 & Rowe 2013, Phillips *et al.*, 2019). In the Gairloch Shear Zone (GSZ), NW Scotland, well-preserved  
65 1019-910 Ma pseudotachylytes potentially record brittle Renlandian deformation (950-940 Ma) that  
66 exploited the fabric of pre-existing Laxfordian (1800-1500 Ma) ductile shear zones, although work  
67 pre-dating the recognition of the Renlandian event in northwest Scotland (Bird *et al.*, 2018) tends to  
68 infer earlier Grenvillian (~1100 Ma) related deformation for brittle GSZ faults (Lei & Park 1993;  
69 Sherlock *et al.* 2008). The pseudotachylytes record foliation-parallel seismic rupture in a variety of  
70 fault plane and damage zone geometries including stepping fault segments, dilational pull-aparts,  
71 branching faults and breccias (e.g. Park 1961). However, the context of the ancient seismicity that  
72 they record has not so far been comprehensively investigated.

73 In this contribution, we detail the record of propagating multi-segment and branching seismic  
74 ruptures and the related formation of dilational sites which are captured in these pseudotachylytes.  
75 In addition, we estimate source parameters for the seismicity recorded in these rocks.

## 76 Seismic slip in the Gairloch Shear Zone

### 77 *Development of the Gairloch Shear Zone*

78 The Gairloch Shear Zone (GSZ) in NW Scotland (Fig. 1a) consists of a series of Laxfordian high strain  
79 zones recording amphibolite to greenschist facies ductile deformation (Droop *et al.* 1999; Park 2010)  
80 and subsequent greenschist facies brittle deformation (Lei & Park 1993). The high strain zones are  
81 typically localised along lithological boundaries within the Loch Maree Group (LMG), a belt of  
82 Paleoproterozoic oceanic meta-basalts, meta-sedimentary rocks and meta-granodiorite (Fig. 1a)

83 interpreted as a 2.0-2.2 Ga island arc and accretionary complex from the Nagssugtoqidian–Lapland–  
84 Kola collisional belt (Whitehouse *et al.* 1997; Park *et al.* 2001). The LMG is incorporated into the  
85 Gairloch Terrane and ‘southern region’ of the Lewisian Complex (Kinny *et al.* 2005).

86 Lithologies affected by the high strain zones and brittle deformation include (Park *et al.* 2001): (a) a  
87 layered suite of metasedimentary rocks, predominantly consisting of quartz-biotite semipelites with  
88 minor contributions of calc-silicate-, quartzitic-, amphibolitic-, chloritic- and graphitic- schists; (b)  
89 hornblende-plagioclase amphibolites, of which the larger bodies are meta-volcanics and the smaller  
90 bodies metamorphosed Scourie Dykes; (c) Archean quartzo-feldspathic orthogneisses from the  
91 basement of the LMG; (d) Paleoproterozoic quartzo-feldspathic orthogneiss, locally with variable  
92 mafic composition. The amphibolites, which form the host rock to the faults discussed in this current  
93 contribution, are typically dominated by hornblende with andesine-oligoclase plagioclase plus minor  
94 and variable quartz, epidote, garnet, biotite and calcite (Park 1966).

95 Polyphase development of the viscous shear zones in the GSZ is thought to have occurred between  
96 1800-1500 Ma (Moorbath & Park 1972, Lei & Park 1993; Park *et al.* 2001). The major phases of this  
97 Laxfordian shear zone formation involved coeval amphibolite facies metamorphism, NW-SE  
98 elongation, dextral and sinistral shear on complementary structures and a progressive steepening  
99 and/or folding of structures (Lei & Park 1993). The subsequent late- and post-Laxfordian brittle  
100 deformation was predominantly sinistral (Lei & Park 1993; Beacom *et al.* 2001), and included the  
101 coseismic generation of pseudotachylytes (Park 1961; Sherlock *et al.* 2008). Late greenschist facies  
102 retrogression is thought to have preceded the onset of brittle deformation (Lei & Park 1993).  
103 Particularly intense bands of brittle fracturing and faulting were initially termed ‘crush zones’ (Peach  
104 *et al.* 1907) and generally follow the NW-SE foliation of the shear zones, mapped as the Leth-  
105 Chreige, Creag Bhan, Flowerdale, Tor an Easain, and Ialltaig - Mill na Claise belts (Lei & Park 1993).  
106 Brittle faulting preceded the deposition of the Stoer Group sediments, and  $^{40}\text{Ar}$ - $^{39}\text{Ar}$  dating of the

107 pseudotachylytes in the Leth-Chreige crust belt date the seismicity there as  $910 \pm 19$  to  $1019 \pm 19$   
108 Ma (Sherlock *et al.* 2008).

109 Pseudotachylytes within the brittle faults (Figs. 1b,c) were first identified by Park (1961), who  
110 confirmed their origin in frictional melting along brittle faults from observations of quench  
111 crystallization textures including spherulites and microlites. These observations pre-dated the  
112 understanding that pseudotachylytes were specifically generated by seismic slip (Sibson 1975;  
113 Cowan 1999; Rowe & Griffith 2015). Observations of pseudotachylytes within the GSZ have generally  
114 been confined to the crush belts along the boundaries between lithological units but also in isolated,  
115 heavily fractured regions within the gneisses and metapelites (Park 1961). Although the crush belts  
116 exploit boundaries with amphibolites, pseudotachylytes have so far only been described from within  
117 the gneisses and the metasedimentary rocks, with Park (1961) interpreting the amphibolites to have  
118 deformed via creep along the foliation. However, Beacom *et al.* (2001) characterise widespread  
119 foliation-parallel fracturing and cataclasites within the amphibolites, suggesting that frictional failure  
120 was accommodated within all lithologies.

#### 121 *Significance of pseudotachylytes in the Gairloch Shear Zone amphibolites*

122 Contrary to previous studies of pseudotachylyte bearing faults in the Gairloch Shear Zone (Park  
123 1961; Sherlock *et al.* 2008), we have focussed on the pseudotachylyte-bearing faults hosted in the  
124 foliated amphibolites of the Loch Maree Group. Amphibolite-hosted pseudotachylytes in the GSZ  
125 offer insights into the effects of pre-existing foliation on rupture geometry, as well as revealing the  
126 influence of an amphibole-dominated lithology. In contrast to many well studied pseudotachylyte-  
127 bearing exhumed fault zones hosted within felsic to intermediate plutonic rocks and weak-to-  
128 moderately foliated quartzo-feldspathic gneisses, for example the Gole Larghe Fault Zone (Di Toro *et al.*  
129 *et al.* 2005a), Outer Hebrides Fault Zone (Sibson 1975), Mt. Abbot quadrangle, Sierra Nevada, (Griffith  
130 *et al.* 2008), Wenchuan Fault Zone (Wang *et al.* 2015), and the active Nojima Fault Zone (Otsuki *et al.*  
131 2003), the amphibolite lithology and foliation-dominant microstructure make the study of the

132 seismic faults hosted within them novel. The amphibolite lithology hosting these GSZ  
133 pseudotachylytes is not common in reported pseudotachylyte-bearing exhumed fault zones,  
134 although amphibole-bearing metabasics are present in the pseudotachylyte-bearing Ivrea-Verbano  
135 Zone (Techmer *et al.* 1992) and Alpine Fault Zone (Toy *et al.* 2011). The GSZ therefore provides a  
136 rare opportunity to study the geological record of seismic faulting within a lithology which may be  
137 analogous to metamorphosed oceanic crust and subducting slabs (Rowe *et al.* 2005, Phillips *et al.*  
138 2019). Additionally, because amphiboles melt under disequilibrium conditions at significantly lower  
139 temperatures than quartz and plagioclase (Spray 2010), we consider whether this influences the  
140 coseismic evolution of the slipping fault plane. Pseudotachylyte-fault zones hosted in anisotropic  
141 rocks of varying lithologies are not uncommon worldwide, and the geometry of GSZ pseudotachylyte  
142 faults show some similarity to those observed in mylonites in the Norumbega shear zone (Swanson  
143 1988; Price *et al.* 2012) and the Ikertôq Shear Zone (Grocott 1981), and in foliated quartz-biotite  
144 gneisses in the Homestake Shear Zone (Allen 2005) in that the pseudotachylyte-bearing faults in the  
145 GSZ are often near-parallel to the foliation. However, initial observations of common  
146 pseudotachylyte fault geometries in the GSZ (Fig. 2) suggest that branching and linkage of fault  
147 planes typically create some discordance across the foliation. These processes are therefore  
148 significant in exploring how earthquake ruptures propagate in anisotropic rock.

## 149 **Observations**

150 In this study we look in detail at field and microstructural observations of pseudotachylyte faults  
151 from the GSZ to examine how examples of the different fault geometries initially identified in Fig. 2  
152 may represent different processes influencing rupture complexity.

### 153 Host amphibolites and identification of pseudotachylytes

154 The sub-vertical NE-SE dipping amphibolite facies fabric is defined primarily by the shape preferred  
155 orientation of prismatic hornblende, whilst quartz and plagioclase tend to be more equant in shape.  
156 Hornblende is typically the most abundant phase, frequently comprising 50-75 % by area, and is also



157 the coarsest phase, with variable grain sizes between 50-1000  $\mu\text{m}$ . In the samples studied here,  
158 quartz and plagioclase are the next most abundant phases. Accessory phases include ilmenite,  
159 apatite, rutile, and titanite, and retrogressive reaction products include epidote, chlorite, biotite and  
160 calcite.

161 Pseudotachylytes hosted in amphibolites are reported here from several localities, all close (within  
162 80 m) to lithological boundaries and/or reported crush zones (Fig. 1a). Within the amphibolites, the  
163 pseudotachylytes share similar characteristics, typically displaying a pale yellow, grey or orange  
164 weathering surface in the field (Fig. 1b), but on fresh surfaces unaltered samples are often pale grey  
165 (Fig. 1c).

166 Pseudotachylytes are identified in thin section by the presence of melt-derived crystalline  
167 microstructures, or by altered assemblages of these features (see Maddock 1983; Kirkpatrick and  
168 Rowe 2013). The crystalline mineralogy of pseudotachylyte matrix – all phases that crystallized from  
169 the melt - hosted within the GSZ amphibolites is predominantly composed of hornblende and  
170 plagioclase with occasional augite. As reported by Park (1961), some GSZ pseudotachylytes have  
171 completely recrystallized to fine-grained biotite and therefore have lost the morphological  
172 characteristics of melt-derived crystallization. In thin section, the pseudotachylyte matrix is typically  
173 dark brown and optically opaque (Figs. 3a,b). Many of the GSZ pseudotachylytes analysed in this  
174 study preserve quench crystallization (or alternatively, devitrification from an initial quenched glass)  
175 crystal morphologies such as dendritic amphibole and plagioclase, radiating crystals of plagioclase  
176 and amphibole nucleating on unmelted survivor clasts (Figs. 3c) or forming spherical radiating  
177 microlites (Figs. 3d). These microlites are formed of the largest crystals in the vein matrix, up to 50  
178  $\mu\text{m}$  in length, but the finer-grained crystalline fraction may be as fine as 2-3  $\mu\text{m}$ . The finer-grained  
179 phases are typically granular or lath-like (Figs. 3c,d). The grain size and morphology of the crystalline  
180 matrix can vary with distance from the vein margin, creating a banded texture (Figs. 3b).

181 Unmelted survivor clasts occur throughout the veins and are usually rounded (Figs. 3a-c). Often  
182 these are monocrystalline and are dominated by quartz, plagioclase (oligoclase), and additionally  
183 apatite and titanite if these are present as accessory minerals in the host amphibolite. Polycrystalline  
184 clasts may also preserve hornblende and biotite (Figs. 3a). In selected examples, clasts of hornblende  
185 appear viscously deformed within a pseudotachylyte matrix that has no obvious solid-state viscous  
186 shear overprint (Figs. 3e), and ductile drag of hornblende is also seen locally adjacent to vein  
187 intersections (Figs. 3f). Within pseudotachylyte fault veins, the ratio of unmelted clasts to the  
188 crystalline melt-derived matrix has a mean value of  $0.11 \pm 0.08$  (2 s.d.). Higher proportions of clasts  
189 seem to be associated with pseudotachylyte veins which are lighter brown in plane light, whereas  
190 low fractions occur in darker coloured matrices.

#### 191 Macroscale geometry of pseudotachylyte veins

192 The simplest fault geometry observed in GSZ pseudotachylyte veins is a pseudotachylyte vein along  
193 an isolated planar fault which may display off-fault intrusions known as injection veins (Fig. 2a).  
194 These occur with a variety of aspect ratios and may curve (Fig. 1b), but they are defined by tensile  
195 fracture opening, in contrast to the shear fracture mode of the fault vein. Many GSZ pseudotachylyte  
196 faults, however, diverge from this basic configuration.

#### 197 *Segmented veins and overstepping*

198 In places, pseudotachylyte fault veins parallel or sub-parallel to the amphibolite foliation form short  
199 sections which are linked by a step across foliation planes over separations of up to 2 cm  
200 centimetres (Figs. 2b,c, 4a). Not all of these pseudotachylyte fault veins are fully linked over the step,  
201 and instead are preserved as separate fault segments (Fig. 4b,c). In the example illustrated in Fig. 4,  
202 parallel fault vein segments overlap by  $\sim 1$ cm and show a pronounced curve at the tips inward  
203 towards the adjacent segment. Fig. 4c indicates narrow band of cataclased amphibolite has been  
204 partially overprinted by the central fault vein segment, which does not follow the band completely  
205 but instead curves up towards the adjacent fault vein segment. Micron-scale shear zones continue

206 beyond the curved vein tips, propagating onwards towards the adjacent vein in the form of a ductile  
207 fault-tip process zone (Fig. 4c-e). At other stepover sites within the same fault, the faults have linked  
208 and a through-going step in the vein is preserved (Fig. 4a,c). These linked steps often leave an  
209 abandoned segment tip, where only one fault segment completes the linkage across the step and  
210 the other is left as a straight overstep (Fig. 4c). The stepovers linked by a single tip are therefore  
211 typically narrower than the one in the upper half of Fig. 4c, where both segment tips have curved  
212 towards the adjacent segment. In a differing overstep-related geometry, rhombohedral pull-apart  
213 structures (Fig. 2c) have formed between overlapping pseudotachylyte fault segments, and may  
214 contain some centimetre-scale rounded clasts of the amphibolite (Fig. 5a).

215 Linkage of two parallel pseudotachylyte fault planes may be a systematic process along longer fault  
216 lengths, as in Fig. 2d. At the locality in Fig. 5b, pale pseudotachylyte occurs in planar veins in two  
217 dominant orientations, one parallel to the foliation and the other discordant. Both are restricted to  
218 an elongate tabular region around 10 cm wide with oblique foliation, bounded by planar  
219 discontinuities that locally also contain pseudotachylyte ('boundary faults', Fig. 5b). The oblique  
220 foliation and shear band structure in the amphibolite can be more clearly seen in the top left of Fig.  
221 5c, in a locality where only a small volume of pseudotachylyte has formed. Internal veins within the  
222 shear band and discordant to the shear band foliation (Fig. 5b) appear to be minor faults with  
223 extensional sense of slip, based on the dilational accumulation of pseudotachylyte above the  
224 hanging wall of an internal fault. It is unclear if the internal foliation-parallel veins have any shear  
225 displacement across them. The discordant internal pseudotachylyte faults typically form an angle of  
226  $\sim 55^\circ$  from the boundary faults. In Fig. 5b, the pseudotachylyte is locally continuous across the two  
227 internal vein orientations and across into the boundary faults, but there is also a cross-cutting  
228 boundary between an extensional fault vein and a foliation parallel vein, suggesting that both sets of  
229 internal faults and the pseudotachylyte along them were created synchronously with slip along the  
230 boundary faults during an episode of seismic rupture. In Fig. 5b, a breccia is locally developed in the  
231 internal zone and rotation of the breccia clasts is apparent. Similarly, in the top right of Fig. 5c,

232 variable volumes of pseudotachylyte within the shear band create complex vein networks and  
233 brecciated domains. The lower shear band in Fig. 5c is here completely brecciated, with rounded,  
234 rotated clasts apparently supported by pseudotachylyte matrix.

#### 235 *Branching Faults*

236 Branching faults (Fig. 2e) introduce discordant fault orientations and can be associated with complex  
237 pseudotachylyte vein networks (Figs. 5d-e). Branching faults in the GSZ often display intersections  
238 with an acute angle of 10-30° between the main fault and the secondary fault branch (Figs. 5d-f).  
239 The branch may split the main pseudotachylyte fault so that one fault vein has a thicker layer of  
240 pseudotachylyte than the other branch. The thicker branch may be either concordant or discordant  
241 to the foliation. At the branching tip of the fault in Figs. 5d, a network of small pseudotachylyte veins  
242 lie around the branching fault, forming a wider apparent damage zone than is usually observed  
243 around pseudotachylyte fault veins in the GSZ. In the fault branch in Fig. 5e, injection veins are  
244 developed in the intersection between the two branches, causing flame-like protrusions from the  
245 thicker fault branch. Closely-spaced fault branches may also be linked by brecciated domains (Fig.  
246 5f).

#### 247 Microscale geometry of pseudotachylyte veins

##### 248 *Vein margins*

249 Whilst pseudotachylyte vein margins are generally planar, millimetre-scale stepping of the margins is  
250 common (Figs. 6a,b) which may be associated with sites of fracture and/or cataclasis in the wall-  
251 rock, or injection veins and smaller-scale roughness (Figs. 6a,b). This is distinct from later faulting  
252 which has also offset some of the pseudotachylyte veins, creating a similar stepped appearance.  
253 Preferential melting of the hornblende relative to plagioclase and quartz creates grain scale  
254 roughness and is observed at vein margins and also within polycrystalline clasts, where hornblende  
255 has melted but is surrounded by apparently intact quartz and plagioclase (Figs. 6c,d). Large

256 polycrystalline clasts may be removed from the margin by sidewall shortcut veins, which isolate  
257 blocks from the new vein margin and progressively smooth steps and curves out of the fault walls  
258 (Figs. 3a, 6e). These large clasts are initially little removed from their point of origin, but may be  
259 significantly rotated and exhibit internal faulting and injection of pseudotachylyte, resulting in  
260 progressive size reduction (Fig. 6e).

#### 261 *Injection veins*

262 Small injection veins of pseudotachylyte away from the generation plane vary in geometry at the  
263 microscopic scale. Some stubby varieties appear to follow grain boundaries and may represent the  
264 exploitation of low melting point minerals, whilst others terminate with thin branches (Fig. 6f,g).  
265 Injections also propagate into clasts as well as into the margins and contribute to progressive  
266 fragmentation of the clasts (Fig. 6e). Some injection veins have rough margins, suggesting  
267 modification of the injection walls via melting.

268

## 269 **Discussion**

### 270 Seismic slip in the amphibolites of the Gairloch Shear Zone

271 The pseudotachylytes of the GSZ record frictional melting during seismic slip along faults in the  
272 amphibolites. Source parameters such as displacement, magnitude, and coseismic temperature,  
273 along with the depth of earthquake activity have not previously been attributed for these faults, so  
274 here we discuss what constraints may be placed on the nature of earthquake slip within the GSZ.

#### 275 *Relationship of seismic rupture with foliation and lithology*

276 Within the GSZ, amphibolite-hosted pseudotachylyte-bearing faults are localised close to the  
277 lithological boundaries, but are not recorded along the actual boundary interfaces; indeed, they  
278 occur at distances up to 80 m laterally away from them. Exploitation of these boundary zones is also  
279 seen in pseudotachylyte faults occurring in the other lithologies that host the GSZ (Park 1961).

280 Spacing and orientation of fracturing has been observed to vary between the lithologies of the GSZ,  
281 with amphibolites hosting typically foliation-parallel brittle deformation with a high factor of  
282 clustering (Beacom *et al.* 2001). Such foliation-parallel fracture pattern is replicated in the  
283 pseudotachylyte-bearing faults and is compatible with the understanding that strong anisotropy  
284 tends to guide shear failure orientation, even if it is somewhat misorientated relative to the principal  
285 stress directions (Donath 1961).

286 The amphibolite host rock presents a contrast in the thermal properties of its constituent minerals -  
287 hornblende has a single-crystal melting temperature of 750 °C, whilst quartz and An<sub>30-50</sub> plagioclase  
288 will melt at ~1550° (if melting occurs before the high temperature phase change to β-christabolite)  
289 and ~1350° respectively (Petzold & Hinz 1976; Spray 2010). Under disequilibrium frictional melting,  
290 this leads to preferential melting of the amphibole, which is clearly illustrated by the clast in Figs. 6  
291 c-d. In the wall of the fault, melting of amphibole between preserved quartz and plagioclase has led  
292 to increased roughness of the fault surface on the grain scale (e.g. Fig. 6b), contrary to mechanical  
293 wear processes that tend to smooth the fault walls with progressive slip (Brodsky *et al.* 2011),  
294 examples of which may also be observed in these pseudotachylytes in the formation of sidewall  
295 shortcuts (Figs. 3a, 6e). Preferential melting of amphibole is also observed in the walls of some  
296 injection veins, indicating that the melt temperature in these off-fault tensile fractures also  
297 remained above 750°C (Spray 2010) and hence was still molten at the tip of the vein, requiring  
298 quenching to be slower than the fracture propagation (Rowe *et al.* 2012).

299 The volumetric ratio of survivor clasts relative to melt-derived matrix within any individual  
300 pseudotachylyte fault vein is an indication of the thermodynamic balance between melting and  
301 mechanical wear processes (O'Hara 2001). In the GSZ pseudotachylytes, the mean 2D clast to matrix  
302 (representing the melt, includes microlites plus the finer-grained crystalline matrix) area ratio is 0.11,  
303 at the lower boundary of the 0.1-0.7 range which has been previously reported for pseudotachylytes  
304 from a collection of different fault zones (O'Hara 2001), indicating that an increased proportion of

305 melt was generated relative to products created purely by mechanical wear during slip. The  
306 breakdown of rock via mechanical wear and melting is influenced by the mineral yield strengths and  
307 thermal energy needed for melting, respectively. Although the ratio of these properties is fairly  
308 constant for many common minerals, amphiboles, particularly hornblende, have slightly lower  
309 melting points relative to their strength (O'Hara 2001; Spray 2010). Therefore, frictional melting of a  
310 hornblende-rich rock might be expected to generate an increased volume of melt along the fault  
311 relative to the volume of unmelted clasts, in comparison to a quartzo-feldspathic lithology.  
312 Additionally, even low coseismic temperature rises, associated with small increments of seismic slip,  
313 may still allow for widespread melting of the amphiboles. This relative ease of coseismic melt  
314 production may have implications for fault structure, with high melt pressures (i.e. fluid pressure)  
315 potentially contributing to opening tensile off-fault cracks (Swanson 1992) alongside dynamic  
316 rupture-tip stress fields (Di Toro *et al.* 2005b; Griffith *et al.* 2009; Ngo *et al.* 2012) and exploitation of  
317 pre-existing fractures. Interaction of locally high fluid pressure along the fault plane with the opening  
318 of dilational sites controlled by fault geometry will drive high fluid pressure gradients and  
319 consequential rapid flow of melt towards the dilational zone, potentially causing brecciation (Sibson  
320 1975; Bjørnerud & Magloughlin 2004), all within the duration of coseismic slip. Hence, the  
321 interaction of the lithological control on melting and the foliation control on fault geometry has  
322 implications for the relative contributions of coseismic fault plane processes to the seismic energy  
323 budget and structural development of the fault zone.

#### 324 *Depth and temperature conditions of seismic faulting in the GSZ*

325 The depth of brittle faulting and seismicity in the GSZ is not well constrained but occurred within  
326 lower greenschist facies temperatures (Park *et al.* 1987; Beacom *et al.* 2001) giving a likely ambient  
327 rock temperature between 250-350°. The geothermal gradient has been estimated for the GSZ as  
328  $22^{+7}_{-4}$  °C km<sup>-1</sup> during Laxfordian ductile deformation phases (Droop *et al.* 1999). Whether this was still  
329 the case for the later brittle phase is not clear, but as Droop *et al.* (1999) regard this as a moderate

330 estimate for stable Precambrian crust, and considering the errors and the time-gap, we use an  
331 approximation of 25°C km<sup>-1</sup> as the geothermal gradient in calculations. This gives a depth range of 9-  
332 13 km for the ambient temperature range 250-350°C.

### 333 *Coseismic fault temperature, displacement, magnitude and slip direction*

334 Pseudotachylyte-bearing faults in the GSZ capture individual episodes of seismic slip, thus capturing  
335 elements of the source parameters of the individual earthquakes. The energy budget required to  
336 melt a given volume of the host rock allows the coseismic heat rise in particular to be estimated, and  
337 is related to the seismic displacement, which scales with the seismic magnitude. Direct  
338 measurement of displacement in the field is not routinely possible in the GSZ, because there are few  
339 markers within the amphibolite that may be cut and offset across the faults. Calculating the  
340 necessary displacement required to produce a certain volume of pseudotachylyte melt is therefore a  
341 useful estimate on the magnitude of earthquake displacement recorded on these faults. The volume  
342 of coseismic melt is approximated by the average thickness of a pseudotachylyte fault vein (Di Toro  
343 *et al.* 2005a). Thickness measurements are best undertaken across fault veins with constant  
344 thickness and limited melt loss into sites such as injection veins and breccia. Although such  
345 geometrically simple veins are not common in the GSZ, a typical thickness of the pseudotachylyte  
346 along linear faults is around 5 mm (e.g. Fig. 4a). The relationship between the thickness of melt, the  
347 displacement and the thermal properties of the rock is

$$348 \quad d = \frac{\rho \cdot w}{\tau} [(1 - \phi)H + c_p(\Delta T)] \quad (1)$$

349 where d is the displacement, ρ the density, w the width of the vein, τ is the shear stress on the fault,  
350 φ is the area of clasts in the vein as a fraction of the total vein, H is latent heat of melting, c<sub>p</sub> is the  
351 specific heat and ΔT is the difference between the coseismic melt temperature and the ambient  
352 temperature before and after the earthquake, T<sub>melt</sub> - T<sub>ambient</sub> (Di Toro *et al.* 2005a). Values used for  
353 these parameters are given in Table 1. Values for the shear stress resolved along the fault are



354 estimated from the lithostatic stress state by equating the lithostatic stress ( $P_c = \rho \cdot g \cdot h$ , where  $g$  is  
355 gravitational acceleration, and  $h$  is depth) with the mean stress of a strike-slip stress field. Assuming  
356 a Poisson's ratio of 0.25 (Jaeger & Cook 1979) and an angle of  $30^\circ$  between the maximum principal  
357 stress and the fault plane, this places the expected range of resolved shear stress at 107-155 MPa for  
358 the estimated depth range of 9 to 13 km (Fig. 7a). Constraining  $\Delta T$  relies on estimating the maximum  
359 temperature reached by the coseismic melt ( $T_{\text{melt}}$ ), which in many pseudotachylytes is reported  
360 within the range  $\sim 1000\text{-}1500^\circ\text{C}$  (O'Hara 2001; Di Toro & Pennacchioni 2004; Caggianelli *et al.* 2005;  
361 Nestola *et al.* 2010) from a combination of thermal and thermodynamic modelling, matrix indicator  
362 phases and melting temperatures of surviving clasts relative to melted phases. For the GSZ  
363 pseudotachylytes we use the latter method, which places upper and lower bounds on the melt  
364 temperature. The lower bound for the melt temperature is  $750^\circ\text{C}$ , the melting temperature of  
365 hornblende. Plagioclase is partially preserved as unmelted survivor clasts, placing a reasonable  
366 upper bound for coseismic fault plane temperature at the  $\text{An}_{30-50}$  melting temperature of  $1350^\circ\text{C}$   
367 (Spray 2010). Using these parameters in equation 1, the resulting mean values of coseismic  
368 displacement equivalent to a pseudotachylyte thickness of 5 mm range from  $d = 123 \pm 40$  mm at 9  
369 km depth to  $d = 76 \pm 28$  mm at 13 km depth (Fig. 7b), scaling inversely with depth-dependent shear  
370 stress.

371 Earthquake magnitude for these events may be loosely constrained based on this displacement  
372 range. The seismic moment,  $M_0$ , is related to the displacement ( $d$ ), rupture area ( $A$ ) and the shear  
373 modulus ( $G$ ) as  $M_0 = d \cdot A \cdot G$ . The typical rupture size on pseudotachylyte faults in the GSZ is  
374 somewhat uncertain, because the pseudotachylyte extent may represent only part of a larger fault  
375 plane that is not always fully exposed or easily traced (Kirkpatrick *et al.* 2012), especially if faults are  
376 foliation parallel and/or segmented. Rupture area is calculated from fault length based on the  
377 assumption of a circular fault with diameter equivalent to the fault length, a simplification of the  
378 elliptical geometry solution demonstrated by Eshelby (1957). A reasonable range of GSZ fault lengths  
379 (i.e. a maximum rupture length) would be between 1m and 100m, in which case the range of

380 moment magnitudes ( $M_w$ ) converted from the seismic moment would be between 0.1 and 3.1  $M_w$   
381 based on the empirical relationship  $M_w = \frac{\log M_0}{1.5} - 6.07$  (Kanamori & Brodsky 2004). The  
382 uncertainties arising from the unknown fault length are clearly large (Fig. 7b), but nonetheless  
383 illustrate that the many of the pseudotachylytes in the GSZ were generated by a series of relatively  
384 small magnitude earthquakes.

385 The slip direction of the brittle faults in the GSZ is typically thought to have been sinistral (Park *et al.*  
386 1987; Beacom *et al.* 2001; Sherlock *et al.* 2008). The sense of slip on the pseudotachylyte faults  
387 presented here is frequently difficult to determine, but where evidence for slip direction exists there  
388 are also dextral examples (e.g. Fig. 5a), indicating that seismicity likely occurred with both apparent  
389 dextral and sinistral kinematics. This is not incompatible with a dominantly sinistral tectonic regime,  
390 because small ruptures that occur as aftershocks or which occur in the damage zone or even further  
391 away from the major fault planes are often observed to have varying slip senses in observations of  
392 present day seismicity (Cheng *et al.* 2018; Cooke & Beyer 2018).

### 393 Rupture geometry and dilational zones

#### 394 *Segmentation and branching*

395 A common feature along GSZ pseudotachylyte-bearing faults is a stepover between parallel but  
396 laterally offset segments of the fault (e.g. Fig. 4, Fig. 5a, Fig. 8a-b). These macroscopically stepped  
397 faults represent linkage of several fault segments, which, in the examples seen, tend to lie parallel to  
398 the amphibolite foliation. There appears to be two mechanisms of linkage between fault segments  
399 containing pseudotachylytes in the GSZ. Firstly, there is linkage driven by curvature of the segment  
400 tips once they overlap with an adjacent segment (Fig. 8a). The best example of this process is  
401 illustrated in Fig. 4. This fault has a number of steps along strike, most of which have a completed  
402 through-going linkage linked and so evidence of the linkage mechanism is obscured. However, in the  
403 stepover detailed in Figs. 4b-e, linkage is not quite complete, and ductile shear zones are preserved  
404 ahead of the fault tips, representing the process zone that precedes a propagating shear fracture

405 (Misra *et al.* 2015). Both the overlapping tips display this process zone (Figs. 4d,e), indicating that  
406 both fault segments were propagating towards the other, in opposing directions (Fig. 8a). The  
407 presence of pseudotachylyte in the fault segments indicates that this propagation occurred during  
408 earthquake rupture, i.e. at least parts of these fault segments were newly formed during the  
409 earthquake which produced the pseudotachylyte, and the interaction of the segment tips indicates  
410 that all the segments must have been actively slipping during the same episode of coseismic rupture.  
411 Where linkage of the segments has occurred at other steps along the fault, the pseudotachylyte is  
412 continuous across the step, indicating that complete linkage of the segments also occurred during  
413 the same earthquake. A further implication is that nucleation of slip occurred at several sites on  
414 adjacent foliation planes, each growing into a short slip segment before a through-going slip plane  
415 was established. This fault therefore records the various stages of centimetre-scale growth,  
416 interaction and linkage of fault segments that can occur within a single earthquake, the duration of  
417 which is typically  $< 0.2$  s for events  $< M_w 3$  (Kanamori & Brodsky 2004). The growth of the through-  
418 going fault in this manner is very similar to the model of fault growth from segments which exploit  
419 pre-existing weaknesses (Segall & Pollard 1983), but in the case of the GSZ the initial weakness plane  
420 is probably the amphibolite foliation, although the apparent overprint of a cataclastic zone by the  
421 pseudotachylyte segment in Fig. 4c may indicate that pre-existing faults were partially exploited by  
422 the later rupture event recorded in the pseudotachylyte. The vein margins are frequently stepped at  
423 smaller scales of  $\sim 1$  mm vein-normal separations (Figs. 6a,b) which suggests that segmentation of  
424 slip may be applicable at several scales, and that on rupture initiation slip may have nucleated  
425 simultaneously across a diffuse suite of foliation planes spaced only a few grains apart. Coalescence  
426 of these would have occurred forming the larger segments typically spaced  $\sim 1$  cm apart (e.g. Fig. 4).  
427 After segment linkage or branching, the fault wall geometry would be liable to be progressively  
428 modified by processes such as the creation of sidewall-shortcuts (Figs. 3a, 6e) which act to smooth  
429 out steps in the vein by by-passing protruding asperities to create a more planar fault margin (Fig.  
430 6e). This rip-out process has been linked specifically to strike-slip faulting along planes of anisotropy

431 (Swanson 1989) but in the GSZ appears to predominantly straighten curved or stepped faults rather  
432 than creating lensoid ramps into the fault walls from an initially planar fault, as in the model of  
433 Swanson (1989), likely due to the segmentation control on the initial fault geometry.

434 The curvature of overlapping segment tips (Fig. 4c) is an expression of the modification of the local  
435 fault tip stress field due to interaction between two closely-spaced overlapping cracks (Pollard *et al.*  
436 1982; Pollard & Aydin 1984; Nicholson & Pollard 1985) which causes the propagation path to curve.  
437 This style of linkage is well-documented in dilatant crack systems including veins and dykes (Pollard  
438 *et al.* 1982; Nicholson & Pollard 1985), in contrast to shear planes which more typically form sets of  
439 secondary fractures and/or folds in the overstep region (Fig. 8b), rather than propagate the primary  
440 crack tips towards each other in this way. The pull-apart in Fig. 5a is an example of a typical  
441 extensional stepover between shear cracks (e.g. Sibson 1986) and is an example of the second  
442 mechanism of fault segment linkage demonstrated in the GSZ pseudotachylytes. In Fig. 5a, the fault  
443 is right-stepping and has an apparent dextral sense of slip, creating an extensional overstep which is  
444 now filled with a pseudotachylyte rhombocasm. These pull-apart stepovers are well documented  
445 between strike-slip fault segments and on releasing bends at all fault scales, from millimetre-width  
446 (Peacock & Sanderson 1995) to hundreds of kilometres (Mann *et al.* 1983), and are also well-  
447 described for pseudotachylyte-bearing faults (e.g. Sibson 1975). Unlike the crack-tip linkage (Fig. 8a),  
448 the multiple parallel slip segments do not necessarily need to exist pre-linkage because transfer of  
449 the rupture across to potential adjacent slip planes (the foliation, in the GSZ amphibolites) may  
450 occur via the formation of secondary faults in the future overstep (Sibson 1986; Harris *et al.* 1991;  
451 Melosh *et al.* 2014). Because this form of linkage is so common, it is interesting that the first  
452 mechanism via propagating crack tips also occurs across these faults, especially when it is more  
453 typical of dilatant mode I cracks (Pollard *et al.* 1982; Pollard & Aydin 1984). Some numerical models  
454 show that this curved propagation of crack tips can also occur on mode II shear fractures (Du &  
455 Aydin 1993; Ando *et al.* 2004). Alternatively, dilation of the fault segments could be introduced via  
456 local high fluid pressure driven by voluminous coseismic melt generation, leading the propagating

457 rupture to behave as hybrid extensional–shear fractures. High coseismic fluid pressure has several  
458 implications for dynamic fault strength, potentially including transient loss of shear strength if the  
459 fluid/melt pressure becomes equal to or greater than the normal stress on the fault. However,  
460 evidence for high melt pressure is typically only locally seen in pseudotachylytes, for example in the  
461 dynamic creation of pseudotachylyte injection veins at the fault tip (Rowe *et al.* 2012; Sawyer &  
462 Resor 2017) and in breccias where extreme rotation of the clasts suggests fluid-supported implosion  
463 (Bjørnerud & Magloughlin 2004). Along relatively simple fault geometries such as that shown in Fig.  
464 4, where off-fault melt escape routes are not apparent, the melt has instead have been trapped  
465 along the fault plane, forming a continuous film and influencing dilatant-crack geometries across the  
466 propagating fault segments. Whichever the mechanism of segment linkage, the resultant stepped  
467 fault geometry is also observed in kilometre scale active fault zones and in earthquake surface  
468 rupture patterns (Tchalenko & Berberian 1975; Bilham & Williams 1985), indicating that some of the  
469 processes of fault linkage observed in the GSZ pseudotachylytes could be potentially up-scaled.  
470 However, the influence and interaction of coseismic melt-pressure and closely-spaced rupture tip  
471 stress fields are perhaps not so easy to simply scale up across larger spatial distances.

472 Branching faults are common in the GSZ (Figs. 5d,e) and represent synchronous seismic slip on both  
473 branches where the pseudotachylyte is continuous across the branch intersection (Rowe *et al.*  
474 2018). Such branching is a recognised feature of kilometre-scale fault zones and can also be linked  
475 on that scale to single earthquake ruptures (Poliakov *et al.* 2002; Fliss *et al.* 2005). Without good  
476 evidence for sense of displacement across the GSZ faults it is difficult to interpret the kinematics of  
477 these branches, as numerical models suggest that branching in both forward and backwards  
478 directions relative to the direction of rupture propagation is possible (Fliss *et al.* 2005). As noted by  
479 Rowe *et al.* (2018), intersecting branches that slip in the same rupture must also experience  
480 different slip vectors and magnitudes of slip, so that the geometry has a direct influence on the  
481 spatial heterogeneity of rupture source properties. In the observations of Rowe *et al.* (2018), two  
482 thin fault branches coalesce into the wider main fault plane. We observe some additional detail by

483 noting that one fault branch is typically wider than the other (Figs. 5d,e), which may signify that  
484 relative differences in seismic slip speed or magnitude, and hence melt production, are common  
485 between coalescing branches. In the case of the branch in Fig. 5e, the discordant branch has a  
486 thicker pseudotachylyte vein and also appears to be longer than the other fault branch which forms  
487 an extension to the main fault vein and remains parallel to the foliation. Ruptures exploiting a pre-  
488 existing fault branch can sometimes terminate rupture on the main fault branch if the secondary  
489 branch has significant length and is inclined at a shallow angle to the main fault (Bhat et al., 2007), as  
490 in Fig 5e. Typically, this termination of rupture on the main fault occurs when the branch is situated  
491 in the extensional field of the propagating rupture tip (Bhat et al., 2007). This branch configuration  
492 might also encourage the development of tensile veining (Fig. 5e) and dilational brecciation (Fig. 5f)  
493 in the intersection of the fault branches, given accommodating slip on the secondary branch. In the  
494 cited models of branching faults (Fliss et al., 2005, Bhat et al., 2007) the secondary fault branches  
495 must exist as a pre-existing structure before the rupture in question is generated along the fault.  
496 Similarly, in cases such as Fig. 5e, where the secondary fault branch is discordant to the foliation, we  
497 suggest that some pre-existing heterogeneity within the amphibolite fabric may be necessary to  
498 divert the rupture down the secondary fault branch and away from the dominant plane of weakness  
499 formed by the foliation. In Fig. 5f, and also in Figs. 5b-c, branching faults within the confines of a  
500 paired fault zone are observed, in the sense that slip on the 'internal' faults is coeval and continuous  
501 with slip on the boundary faults, as indicated by brecciation in the branch intersection (Fig. 5f).  
502 However, in these cases the length of the secondary fault branch (the internal fault) is limited by the  
503 width of the controlling structure (the shear band), and so branching of the rupture along these  
504 small faults is unlikely to inhibit the continuing rupture along the main boundary fault, whatever the  
505 configuration of the secondary branch faults with respect to the main fault and stress field (Bhat et  
506 al., 2007).

507 *Brecciation sites*

508 Within the GSZ pseudotachylytes, there are several examples of localised dilation associated with  
509 coseismic slip and pseudotachylytes. These dilational sites are controlled by the fault geometry.  
510 Under the classification scheme of (Rowe *et al.* 2018), these can be described as angular breccias  
511 (Fig. 5f), pull-aparts/rhombocasms (Fig. 5a), and tabular breccias (Fig. 5c). The pseudotachylyte faults  
512 in the GSZ show progressive stages of breccia development, which illustrate how these features  
513 evolve (Fig. 8).

514 Angular breccias are associated with dilational sites within the intersections of branching faults (Fig.  
515 5f), although they may potentially also form between oblique adjacent fault segments. In both  
516 cases, they signify coeval seismic slip on the bounding structures. Pull-aparts filled with  
517 pseudotachylyte may contain breccia clasts (Fig. 5a) and in the case of rhombocasms are typically  
518 formed by dilation at extensional stepovers between fault segments. These rhombohedral pull-  
519 aparts form via secondary tensile and shear fractures which form the through-going link between  
520 overlapping faults (Fig. 8b), and do not necessarily require fluid (including melt) to fragment the rock  
521 in the overlap (Sibson 1986; Melosh *et al.* 2014) although high fluid pressures may assist this process  
522 (Sibson 1975; Bjørnerud & Magloughlin 2004). A similar final geometry is formed via the crack-tip  
523 propagation mechanism of segment linkage, where the isolation of a 'bridge' between curving,  
524 overlapping fault tips and the resultant influx of melt might induce tensile fragmentation of the  
525 bridge (Fig. 8a) once it is surrounded by melt and confinement is lost (Nicholson & Pollard 1985). The  
526 resulting breccia geometry would be defined by the curvature of the fault segments, likely producing  
527 a more rectangular stepover breccia than the rhombohedral pull-aparts (Figs. 8a,b).

528 The tabular pseudotachylyte breccias in the GSZ portray clearly how these structures progressively  
529 form within a single earthquake (Fig. 8c). A pre-existing shear band has been reactivated by  
530 concurrent slip on both boundaries, with exploitation of the internal oblique foliation for  
531 pseudotachylyte injection and/or potential shearing (Fig. 5b). The geometry of this stage is very  
532 similar to the 'strike-slip duplexes' observed in the Ikertôq Shear Zone, Greenland (Grocott 1981)

533 and the Norumbega Shear Zone, US (Swanson 1988) where internal Riedel shear sets are a product  
534 of interaction between the paired boundary faults and also may contain pseudotachylyte, as in the  
535 GSZ examples. The offset on these internal faults implies that they are not a product of dynamic  
536 tensile fracture as in the brecciation model of Melosh *et al.* (2014). In the GSZ the internal faults are  
537 extensional and orientated at a moderately high angle to the boundary faults, suggesting that they  
538 could be X-type Riedel shears which tend to indicate layer-parallel extension (Swanson 1988). This  
539 condition is considered ideal for the progressive formation of breccias from paired fault zones  
540 (Swanson 1988), which requires a combination of increasing internal fault formation combined with  
541 increasing volumes of melt in the internal zone until catastrophic fragmentation brecciates domains  
542 of the rock (Fig. 8c). In order for the paired fault zones to form, an anisotropic rock is thought to be  
543 necessary, with Swanson (1988) suggesting that these may mainly form in mylonites near the base  
544 of the seismogenic zone. However, the foliation in the Gairloch amphibolites, primarily defined by  
545 parallel orientation of prismatic amphiboles, also provides an appropriate fabric, especially where  
546 reinforced by pre-existing structural heterogeneities such as shear bands. Paired fault zones may  
547 therefore be a feature, at least at this centimetre to metre scale, of any level in the brittle crust  
548 where systematic anisotropy is present.

549 The presence of foliation also favours the progression to fragmentation and breccia formation due  
550 to preferential utilisation of the foliation planes for fracturing (Melosh *et al.* 2014) and in the GSZ  
551 this is supported by the injection of pseudotachylyte along the internal foliation planes (e.g. Fig. 5b).  
552 It is not clear, however, whether this rupture geometry would be a feature of large tectonic scale  
553 earthquakes. Riedel shears may form part of large ruptures (e.g.  $M_w$  7.8 Kunlun earthquake, Lin and  
554 Nishikawa 2011), and strike slip duplex geometries with paired boundary fault zones are observed at  
555 5-10 km scales (Cembrano *et al.* 2005). However, the synchronous propagation of rupture both  
556 along parallel segments (i.e. the paired boundary faults) has so far not been identified in active  
557 earthquakes (Rowe *et al.* 2018). The mechanisms allowing the paired faults to propagate past each  
558 other, rather than form linked stepovers similar to Fig. 8a, is therefore of interest, although once



559 the paired slip planes are in motion the process of forming the internal dilational pull-apart is  
560 probably much the same (Sibson 1975; Cembrano *et al.* 2005). Such rupture geometries may  
561 therefore be closely controlled by the spacing between the two faults (Harris *et al.* 1991; Ando *et al.*  
562 2004) along with the favourability of the initial slip planes (Donath 1961). The aspect ratio of these  
563 elongate structures is such that even if scaled up to tens of kilometres, the separation between the  
564 boundary faults might be unresolvable at the spatial resolution of seismological observations or  
565 from geodetic observations of surface deformation.

#### 566 Context of seismicity recorded by pseudotachylytes in the GSZ

567 The GSZ records ~1 Ga seismicity hosted within foliated amphibolites and other lithologies. In the  
568 amphibolites, the pseudotachylytes were formed by small magnitude ( $\leq M_w$  3) earthquake ruptures  
569 that frequently exploited the foliation within the host rock, but which have locally also branched,  
570 stepped and brecciated volumes of the rock. These faults are scattered close to the lithological  
571 boundaries which were thought to localise most of the brittle deformation (Lei & Park 1993), but no  
572 pseudotachylytes in this study have been found to lie in the core of the crush belts along the actual  
573 lithological interface itself, instead typically forming small fault clusters within ~100 m of the  
574 boundary. It is expected that earthquakes would also rupture along the major heterogeneity of the  
575 lithological boundaries, especially where the intensely fragmented 'crush zones' are observed (Fig.  
576 1a), but repeated slip episodes combined with potential fault-focussed fluid influx and subsequent  
577 alteration would likely fragment and overprint any pseudotachylyte produced there, making them  
578 unrecognisable (Kirkpatrick & Rowe 2013). Many of these pseudotachylytes record a single episode  
579 of slip, with only a couple of examples showing that an older pseudotachylyte has been cut through  
580 by a later pseudotachylyte-bearing fault, or that a pseudotachylyte overprints cataclasite (e.g. Fig.  
581 4c). This suggests that each new earthquake preferentially ruptured along a new fault plane, likely  
582 because solidified pseudotachylytes tend to strengthen the fault planes they occur on within the  
583 upper crust (Mitchell *et al.* 2016; Hayward & Cox 2017) if they avoid wholesale hydration and

584 alteration to phyllosilicate-rich assemblages (Phillips et al., 2019). A possible model for these small  
585 pseudotachylyte faults observed here would be scattered seismic slip occurring in the damage zone  
586 of the principal slip plane along the lithological boundaries, much as has been suggested for  
587 pseudotachylytes in exhumed sections of the Alpine Fault, New Zealand (Toy *et al.* 2011).

588 These pseudotachylytes record seismicity along brittle faults that occurred between 1019 and 910  
589 Ma (Sherlock et al., 2008). Previous discussion of these dates found that there was not enough  
590 resolution to distinguish whether the seismicity was a feature of late-Grenvillian or of post-  
591 Grenvillian deformation (Sherlock et al., 2008). However, more recent recognition of the Valhalla  
592 orogeny (1030-710 Ma) in the North Atlantic and, more specifically, its 980-910 Renlandian phase  
593 (Cawood et al., 2010) provide a better fit to the pseudotachylyte ages of the GSZ. The metamorphic  
594 signature of the Renlandian has recently been reported from Neoproterozoic Morar Group  
595 metasedimentary rocks in NW Scotland (Bird et al., 2018), although prior to their Caledonian  
596 transport in the hanging wall of the Moine Thrust (435-420 Ma, Streule et al., 2010) these  
597 metasediments may have lain an additional ~80 km or more away from the GSZ (Elliot and Johnston,  
598 1980). Meanwhile, Neoproterozoic Torridon group sediments unconformably deposited around  
599 1080-980 Ma (Turnbull et al., 1996, Rainbird et al., 2001) onto the GSZ and the Loch Maree Group  
600 (Fig. 1) are not metamorphosed. This would imply that, if the GSZ pseudotachylytes do represent  
601 Renlandian deformation, that seismicity took place not much deeper than around 6 km, the  
602 maximum known depositional thickness of the Torridon Group (Stewart, 2002) and the maximum  
603 identified depth of burial of basal Torridon Group paleosols prior to the initiation of Caledonian  
604 thrusting (Williams, 2015). This is shallower than the 9-13 km depth range for pseudotachylyte  
605 generation estimated earlier in the discussion, although this estimation carried large uncertainty.  
606 Another issue is that no pseudotachylytes or related faults are observed in the overlying Torridon  
607 Group, requiring the basement and cover to have been completely uncoupled. This observation  
608 previously led workers to infer that the pseudotachylytes pre-dated sediment deposition, but the  
609 Applecross formation of the Torridon Group, also present in the GSZ area, is observed to have a low

610 elastic modulus (which would have been still lower prior to sediment consolidation) which could  
611 make it resistant to brittle failure (Ellis et al., 2012). Hence, they may not record obvious indicators  
612 of propagation of the seismic failure from the underlying GSZ, especially if, as is implied here, the  
613 seismicity was characterised by small-length scale, small magnitude earthquake ruptures. However,  
614 further uncertainty as to the relative timing and context of seismic, pseudotachylyte-generating  
615 faulting on the GSZ is presented by observations that the pseudotachylytes are cut by late normal  
616 faults (Sherlock et al., 2008) that are thought to be associated with extension related to the  
617 deposition of the Torridonian sediments (Beacom et al., 1999). More detailed field characterization  
618 of fault and fracture age relationships is needed in order to clarify this remaining uncertainty in  
619 timing and regional context of the seismicity.

620 Despite their age and small length scales, the pseudotachylytes in the amphibolites of the GSZ are  
621 well preserved and capture complex geometries and interactions of earthquake ruptures within  
622 anisotropic rock. It is important to recognise the controls on how these rupture geometries might  
623 have formed at all scales, because they display the conditions under which seismic rupture can  
624 propagate, or alternatively be arrested by, regions of geometrical complexity and separation along  
625 faults (Sibson 1985; Harris *et al.* 1991). Additionally, there has been increased recognition of  
626 complex ruptures with synchronous slip on multiple fault strands occurring in large recent  
627 earthquakes (e.g. Fletcher et al. 2016; Hamling et al. 2017; Ruppert et al. 2018). Understanding the  
628 controls on such ruptures can be enhanced by studying the geological record of seismicity in  
629 exhumed fault zones such as the GSZ.

## 630 **Conclusions**

631 The geometry of small-scale pseudotachylyte-bearing faults in the Gairloch Shear Zone record  
632 rupture geometries that are comparable with those of kilometre-scale large magnitude earthquakes.  
633 This geometry is influenced by the anisotropy of the foliation within the hosting amphibolites, and  
634 potentially also by the high coseismic fluid pressures that might result from voluminous frictional

635 melting of a lithology dominated by low melting point amphibole. A homogeneously distributed  
636 foliation led to multiple points of slip nucleation and a segmented fault structure during early  
637 rupture, followed by the interaction and linkage of adjacent segments as slip progressed. The  
638 interplay with high coseismic melt pressures may be evident in the dilational crack style of segment  
639 linkage and frequent occurrences of brecciated domains, creating a record of a variety of rupture  
640 geometries.

641

642 **Acknowledgements**

643 LC gratefully acknowledges funding from NERC (Studentship 1228272) and a National Museums  
644 Scotland CASE award which facilitated this work. We are grateful for constructive reviews from Eddie  
645 Dempsey and Joe Allen, which greatly improved the manuscript.

646 **References**

- 647 Allen, J.L. 2005. A multi-kilometer pseudotachylyte system as an exhumed record of earthquake  
648 rupture geometry at hypocentral depths (Colorado, USA). *Tectonophysics*, **402**, 37–54,  
649 <https://doi.org/10.1016/j.tecto.2004.10.017>.
- 650 Allen, J.L., O’Hara, K.D. & Moecher, D.P. 2002. Structural geometry and thermal history of  
651 pseudotachylyte from the Homestake shear zone, Sawatch Range, Colorado. *Field Guides* , **3**,  
652 17–32, <https://doi.org/10.1130/0-8137-0003-5.17>.
- 653 Ando, R., Tada, T. & Yamashita, T. 2004. Dynamic evolution of a fault system through interactions  
654 between fault segments. *Journal of Geophysical Research: Solid Earth*, **109**,  
655 <https://doi.org/10.1029/2003JB002665>.
- 656 Beacom, L.E., Anderson, T.B. & Holdsworth, R.E. 1999. Using basement-hosted clastic dykes as syn-  
657 rifting palaeostress indicators: an example from the basal Stoer Group, northwest Scotland.  
658 *Geological Magazine*, **136**, S0016756899002605,  
659 <https://doi.org/10.1017/S0016756899002605>.
- 660 Beacom, L.E., Holdsworth, R.E., McCaffrey, K.J.W. & Anderson, T.B. 2001. A quantitative study of the  
661 influence of pre-existing compositional and fabric heterogeneities upon fracture-zone  
662 development during basement reactivation. In: Holdsworth, R. E., Strachan, R. A., Magloughlin,  
663 J. F. & Nipe, R. J. (eds) *Nature and Tectonic Significance of Fault Zone Weakening*. Bath,  
664 Geological Soc Publishing House, 195–211., <https://doi.org/10.1144/gsl.sp.2001.186.01.12>.
- 665 Bhat, H.S., Olives, M., Dmowska, R. & Rice, J.R. 2007. Role of fault branches in earthquake rupture  
666 dynamics. *Journal of Geophysical Research: Solid Earth*, **112**,  
667 <https://doi.org/10.1029/2007JB005027>.
- 668 Bilham, R. & Williams, P. 1985. Sawtooth segmentation and deformation processes on the southern  
669 San Andreas Fault, California. *Geophysical Research Letters*, **12**, 557–560,  
670 <https://doi.org/10.1029/GL012i009p00557>.
- 671 Bird, A., Cutts, K., Strachan, R., Thirlwall, M. F., & Hand, M. (2018). First evidence of Renlandian (c.  
672 950–940 Ma) orogeny in mainland Scotland: Implications for the status of the Moine  
673 Supergroup and circum-North Atlantic correlations. *Precambrian Research*, **305**, 283–294.  
674 <https://doi.org/https://doi.org/10.1016/j.precamres.2017.12.019>
- 675 Bjørnerud, M. & Magloughlin, J.F. 2004. Pressure-related feedback processes in the generation of  
676 pseudotachylytes. *Journal of Structural Geology*, **26**, 2317–2323,  
677 <https://doi.org/http://dx.doi.org/10.1016/j.jsg.2002.08.001>.
- 678 Brodsky, E.E., Gilchrist, J.J., Sagy, A. & Collettini, C. 2011. Faults smooth gradually as a function of  
679 slip. *Earth and Planetary Science Letters*, **302**, 185–193,  
680 <https://doi.org/10.1016/j.epsl.2010.12.010>.
- 681 Caggianelli, A., de Lorenzo, S. & Prosser, G. 2005. Modelling the heat pulses generated on a fault  
682 plane during coseismic slip: Inferences from the pseudotachylites of the Copanello cliffs

- 683 (Calabria, Italy). *Tectonophysics*, **405**, 99–119,  
684 <https://doi.org/http://dx.doi.org/10.1016/j.tecto.2005.05.017>.
- 685 Cembrano, J., González, G., Arancibia, G., Ahumada, I., Olivares, V. & Herrera, V. 2005. Fault zone  
686 development and strain partitioning in an extensional strike-slip duplex: A case study from the  
687 Mesozoic Atacama fault system, Northern Chile. *Tectonophysics*, **400**, 105–125,  
688 <https://doi.org/https://doi.org/10.1016/j.tecto.2005.02.012>.
- 689 Cheng, Y., Ross, Z.E. & Ben-Zion, Y. 2018. Diverse Volumetric Faulting Patterns in the San Jacinto  
690 Fault Zone. *Journal of Geophysical Research: Solid Earth*, **123**, 5068–5081,  
691 <https://doi.org/10.1029/2017JB015408>.
- 692 Cooke, M.L. & Beyer, J.L. 2018. Off-Fault Focal Mechanisms Not Representative of Interseismic Fault  
693 Loading Suggest Deep Creep on the Northern San Jacinto Fault. *Geophysical Research Letters*,  
694 **45**, 8976–8984, <https://doi.org/10.1029/2018GL078932>.
- 695 Cowan, D.S. 1999. Do faults preserve a record of seismic slip? A field geologist's opinion. *Journal of*  
696 *Structural Geology*, **21**, 995–1001, [https://doi.org/10.1016/S0191-8141\(99\)00046-2](https://doi.org/10.1016/S0191-8141(99)00046-2).
- 697 Di Toro, G. & Pennacchioni, G. 2004. Superheated friction-induced melts in zoned pseudotachylytes  
698 within the Adamello tonalites (Italian Southern Alps). *Journal of Structural Geology*, **26**, 1783–  
699 1801, <https://doi.org/10.1016/j.jsg.2004.03.001>.
- 700 Di Toro, G. & Pennacchioni, G. 2005. Fault plane processes and mesoscopic structure of a strong-  
701 type seismogenic fault in tonalites (Adamello batholith, Southern Alps). *Tectonophysics*, **402**,  
702 55–80, <https://doi.org/http://dx.doi.org/10.1016/j.tecto.2004.12.036>.
- 703 Di Toro, G., Pennacchioni, G. & Teza, G. 2005a. Can pseudotachylytes be used to infer earthquake  
704 source parameters? An example of limitations in the study of exhumed faults. *Tectonophysics*,  
705 **402**, 3–20, <https://doi.org/10.1016/j.tecto.2004.10.014>.
- 706 Di Toro, G., Nielsen, S. & Pennacchioni, G. 2005b. Earthquake rupture dynamics frozen in exhumed  
707 ancient faults. *Nature*, **436**, 1009–1012,  
708 [https://doi.org/http://www.nature.com/nature/journal/v436/n7053/supinfo/nature03910\\_S](https://doi.org/http://www.nature.com/nature/journal/v436/n7053/supinfo/nature03910_S1.html)  
709 1.html.
- 710 Donath, F.A. 1961. Experimental study of shear failure in anisotropic rocks. *Geological Society of*  
711 *America Bulletin*, **72**, 985–989, [https://doi.org/10.1130/0016-](https://doi.org/10.1130/0016-7606(1961)72[985:ESOSFI]2.0.CO;2)  
712 7606(1961)72[985:ESOSFI]2.0.CO;2.
- 713 Droop, G.T.R., Fernandes, L.A.D. & Shaw, S. 1999. Laxfordian metamorphic conditions of the  
714 Palaeoproterozoic Loch Maree Group, Lewisian Complex, NW Scotland. *Scottish Journal of*  
715 *Geology*, **35**, 31–50, <https://doi.org/10.1144/sjg35010031>.
- 716 Du, Y. & Aydin, A. 1993. The maximum distortional strain energy density criterion for shear fracture  
717 propagation With applications to the growth paths of En Échelon faults. *Geophysical Research*  
718 *Letters*, **20**, 1091–1094, <https://doi.org/10.1029/93GL01238>.
- 719 Elliott, D., & Johnson, M. R. W. (1980). Structural evolution in the northern part of the Moine thrust  
720 belt, NW Scotland. *Transactions of the Royal Society of Edinburgh: Earth Sciences*, **71**(2), 69–96.  
721 [https://doi.org/DOI: 10.1017/S0263593300013523](https://doi.org/DOI:10.1017/S0263593300013523)
- 722 Ellis, M. A., Laubach, S. E., Eichhubl, P., Olson, J. E., & Hargrove, P. (2012). Fracture development and  
723 diagenesis of Torridon Group Applecross Formation, near An Teallach, NW Scotland: millennia  
724 of brittle deformation resilience? *Journal of the Geological Society*, **169**(3), 297 LP – 310.  
725 <https://doi.org/10.1144/0016-76492011-086>

- 726 Eshelby, J. D. (1957). The determination of the elastic field of an ellipsoidal inclusion, and related  
727 problems. *Proceedings of the Royal Society of London A: Mathematical, Physical and*  
728 *Engineering Sciences* **241**, 376–396.
- 729 Ferrand, T.P., Labrousse, L., Eloy, G., Fabbri, O., Hilairet, N. & Schubnel, A. 2018. Energy Balance  
730 From a Mantle Pseudotachylyte, Balmuccia, Italy. *Journal of Geophysical Research: Solid Earth*,  
731 **123**, 3943–3967, <https://doi.org/10.1002/2017JB014795>.
- 732 Fletcher, J.M., Oskin, M.E. & Teran, O.J. 2016. The role of a keystone fault in triggering the complex  
733 El Mayor–Cucapah earthquake rupture. *Nature Geoscience*, **9**, 303.
- 734 Fliss, S., Bhat, H.S., Dmowska, R. & Rice, J.R. 2005. Fault branching and rupture directivity. *Journal of*  
735 *Geophysical Research: Solid Earth*, **110**, <https://doi.org/10.1029/2004JB003368>.
- 736 Griffith, W.A. & Prakash, V. 2015. Integrating field observations and fracture mechanics models to  
737 constrain seismic source parameters for ancient earthquakes. *Geology*, **43**, 763–766,  
738 <https://doi.org/10.1130/G36773.1>.
- 739 Griffith, W.A., Di Toro, G., Pennacchioni, G. & Pollard, D.D. 2008. Thin pseudotachylytes in faults of  
740 the Mt. Abbot quadrangle, Sierra Nevada: Physical constraints for small seismic slip events.  
741 *Journal of Structural Geology*, **30**, 1086–1094,  
742 <https://doi.org/http://dx.doi.org/10.1016/j.jsg.2008.05.003>.
- 743 Griffith, W.A., Rosakis, A., Pollard, D.D. & Ko, C.W. 2009. Dynamic rupture experiments elucidate  
744 tensile crack development during propagating earthquake ruptures. *Geology*, **37**, 795–798,  
745 <https://doi.org/10.1130/G30064A.1>.
- 746 Griffith, W.A., Nielsen, S., Di Toro, G. & Smith, S.A.F. 2010. Rough faults, distributed weakening, and  
747 off-fault deformation. *Journal of Geophysical Research: Solid Earth*, **115**, B08409,  
748 <https://doi.org/10.1029/2009jb006925>.
- 749 Grocott, J. 1981. Fracture geometry of pseudotachylyte generation zones: a study of shear fractures  
750 formed during seismic events. *Journal of Structural Geology*, **3**, 169–178,  
751 [https://doi.org/10.1016/0191-8141\(81\)90012-2](https://doi.org/10.1016/0191-8141(81)90012-2).
- 752 Hacker, B.R., Abers, G.A. & Peacock, S.M. 2003. Subduction factory 1. Theoretical mineralogy,  
753 densities, seismic wave speeds, and H<sub>2</sub>O contents. *Journal of Geophysical Research: Solid*  
754 *Earth*, **108**, <https://doi.org/10.1029/2001JB001127>.
- 755 Hamling, I.J., Hreinsdóttir, S., et al. 2017. Complex multifault rupture during the 2016  
756 &lt;em>&M&lt;/em>&lt;sub>w&lt;/sub>; 7.8 Kaikōura earthquake, New Zealand.  
757 *Science*, **356**.
- 758 Harris, R.A., Archuleta, R.J. & Day, S.M. 1991. Fault steps and the dynamic rupture process: 2-D  
759 numerical simulations of a spontaneously propagating shear fracture. *Geophysical Research*  
760 *Letters*, **18**, 893–896, <https://doi.org/10.1029/91GL01061>.
- 761 Hayward, K.S. & Cox, S.F. 2017. Melt Welding and Its Role in Fault Reactivation and Localization of  
762 Fracture Damage in Seismically Active Faults. *Journal of Geophysical Research: Solid Earth*, **122**,  
763 9689–9713, <https://doi.org/10.1002/2017JB014903>.
- 764 Holland, T.J.B. & Powell, R. 2004. An internally consistent thermodynamic data set for phases of  
765 petrological interest. *Journal of Metamorphic Geology*, **16**, 309–343,  
766 <https://doi.org/10.1111/j.1525-1314.1998.00140.x>.
- 767 Jaeger, J.C. & Cook, N.G.W. 1979. *Fundamentals of Rock Mechanics*, 3rd ed. London, Chapman &  
768 Hall.

- 769 Kanamori, H. & Brodsky, E. 2004. The physics of earthquakes. *Reports on Progress in Physics*, **67**,  
770 1429.
- 771 Kinny, P.D., Friend, C.R.L. & Love, G.J. 2005. Proposal for a terrane-based nomenclature for the  
772 Lewisian Gneiss Complex of NW Scotland. *Journal of the Geological Society*, **162**, 175–186,  
773 <https://doi.org/10.1144/0016-764903-149>.
- 774 Kirkpatrick, J.D. & Rowe, C.D. 2013. Disappearing ink: How pseudotachylytes are lost from the rock  
775 record. *Journal of Structural Geology*, **52**, 183–198,  
776 <https://doi.org/http://dx.doi.org/10.1016/j.jsg.2013.03.003>.
- 777 Kirkpatrick, J.D. & Shipton, Z.K. 2009. Geologic evidence for multiple slip weakening mechanisms  
778 during seismic slip in crystalline rock. *J. Geophys. Res.*, **114**, B12401,  
779 <https://doi.org/10.1029/2008jb006037>.
- 780 Kirkpatrick, J.D., Dobson, K.J., Mark, D.F., Shipton, Z.K., Brodsky, E.E. & Stuart, F.M. 2012. The depth  
781 of pseudotachylyte formation from detailed thermochronology and constraints on coseismic  
782 stress drop variability. *J. Geophys. Res.*, **117**, B06406, <https://doi.org/10.1029/2011jb008846>.
- 783 Lei, S. & Park, R.G. 1993. Reversals of movement sense in Lewisian brittle-ductile shear zones at  
784 Gairloch, NW Scotland, in the context of Laxfordian kinematic history. *Scottish Journal of  
785 Geology*, **29**, 9–19, <https://doi.org/10.1144/sjg29010009>.
- 786 Lin, A. & Nishikawa, M. 2011. Riedel shear structures in the co-seismic surface rupture zone  
787 produced by the 2001 Mw 7.8 Kunlun earthquake, northern Tibetan Plateau. *Journal of  
788 Structural Geology*, **33**, 1302–1311,  
789 <https://doi.org/http://dx.doi.org/10.1016/j.jsg.2011.07.003>.
- 790 Maddock, R.H. 1983. Melt origin of fault-generated pseudotachylytes demonstrated by textures.  
791 *Geology*, **11**, 105–108, [https://doi.org/10.1130/0091-7613\(1983\)11<105:moofpd>2.0.co;2](https://doi.org/10.1130/0091-7613(1983)11<105:moofpd>2.0.co;2).
- 792 Mann, P., Hempton, M.R., Bradley, D.C. & Burke, K. 1983. Development of Pull-Apart Basins. *The  
793 Journal of Geology*, **91**, 529–554, <https://doi.org/10.1086/628803>.
- 794 Melosh, B.L., Rowe, C.D., Smit, L., Groenewald, C., Lambert, C.W. & Macey, P. 2014. Snap, Crackle,  
795 Pop: Dilational fault breccias record seismic slip below the brittle–plastic transition. *Earth and  
796 Planetary Science Letters*, **403**, 432–445,  
797 <https://doi.org/http://dx.doi.org/10.1016/j.epsl.2014.07.002>.
- 798 Misra, S., Ellis, S. & Mandal, N. 2015. Fault damage zones in mechanically layered rocks: The effects  
799 of planar anisotropy. *Journal of Geophysical Research: Solid Earth*, **120**, 5432–5452,  
800 <https://doi.org/10.1002/2014JB011780>.
- 801 Mitchell, T.M., Toy, V., Di Toro, G., Renner, J. & Sibson, R.H. 2016. Fault welding by pseudotachylyte  
802 formation. *Geology*, <https://doi.org/10.1130/G38373.1>.
- 803 Moorbath, S. & Park, R.G. 1972. The Lewisian chronology of the southern region of the Scottish  
804 mainland. *Scottish Journal of Geology*, **8**, 51 LP – 74, <https://doi.org/10.1144/sjg08010051>.
- 805 Nestola, F., Mittempergher, S., Toro, G.D., Zorzi, F. & Pedron, D. 2010. Evidence of dmisteinbergite  
806 (hexagonal form of CaAl<sub>2</sub>Si<sub>2</sub>O<sub>8</sub>) in pseudotachylyte: A tool to constrain the thermal history of  
807 a seismic event. *American Mineralogist*, **95**, 405–409.
- 808 Ngo, D., Huang, Y., Rosakis, A., Griffith, W.A. & Pollard, D. 2012. Off-fault tensile cracks: A link  
809 between geological fault observations, lab experiments, and dynamic rupture models. *Journal  
810 of Geophysical Research: Solid Earth*, **117**, B01307, <https://doi.org/10.1029/2011jb008577>.



- 811 Nicholson, R. & Pollard, D.D. 1985. Dilation and linkage of echelon cracks. *Journal of Structural*  
812 *Geology*, **7**, 583–590, [https://doi.org/https://doi.org/10.1016/0191-8141\(85\)90030-6](https://doi.org/https://doi.org/10.1016/0191-8141(85)90030-6).
- 813 Nissen, E., Elliott, J.R., et al. 2016. Limitations of rupture forecasting exposed by instantaneously  
814 triggered earthquake doublet. *Nature Geosci*, **9**, 330–336.
- 815 O’Hara, K.D. 2001. A pseudotachylite geothermometer. *Journal of Structural Geology*, **23**, 1345–  
816 1357.
- 817 Ohno, I. 1995. Temperature Variation of Elastic Properties of  $\alpha$ -Quartz up to the  $\alpha$ - $\beta$  Transition.  
818 *Journal of Physics of the Earth*, **43**, 157–169, <https://doi.org/10.4294/jpe1952.43.157>.
- 819 Otsuki, K., Monzawa, N. & Nagase, T. 2003. Fluidization and melting of fault gouge during seismic  
820 slip: Identification in the Nojima fault zone and implications for focal earthquake mechanisms.  
821 *Journal of Geophysical Research: Solid Earth*, **108**, 2192,  
822 <https://doi.org/10.1029/2001jb001711>.
- 823 Park, R.G. 1961. The pseudotachylite of the Gairloch District, Ross-shire, Scotland. *American Journal*  
824 *of Science*, **259**, 542–550, <https://doi.org/10.2475/ajs.259.7.542>.
- 825 Park, R.G. 1966. Nature and origin of Lewisian basic rocks of Gairloch, Ross-shire. *Scottish Journal of*  
826 *Geology*, **2**, 179 LP-199.
- 827 Park, R.G. 2010. Structure and evolution of the Lewisian Gairloch shear zone: variable movement  
828 directions in a strike-slip regime. *Scottish Journal of Geology*, **46**, 31–44,  
829 <https://doi.org/10.1144/0036-9276/01-405>.
- 830 Park, R.G., Crane, A. & Niamatullah, M. 1987. Early Proterozoic structure and kinematic evolution of  
831 the southern mainland Lewisian. *Geological Society, London, Special Publications*, **27**, 139–151,  
832 <https://doi.org/10.1144/gsl.sp.1987.027.01.12>.
- 833 Park, R.G., Tarney, J. & Connelly, J.N. 2001. The Loch Maree Group: Palaeoproterozoic subduction-  
834 accretion complex in the Lewisian of NW Scotland. *Precambrian Research*, **105**, 205–226,  
835 [https://doi.org/10.1016/s0301-9268\(00\)00112-1](https://doi.org/10.1016/s0301-9268(00)00112-1).
- 836 Peach, B.N., Horne, J., Gunn, W., Clough, C.T. & Teall, J.J.H. 1907. *The Geological Structure of the*  
837 *North-West Highlands of Scotland*. Glasgow, HM Stationary Office.
- 838 Peacock, D.C.P. & Sanderson, D.J. 1995. Pull-aparts, shear fractures and pressure solution.  
839 *Tectonophysics*, **241**, 1–13, [https://doi.org/https://doi.org/10.1016/0040-1951\(94\)00184-B](https://doi.org/https://doi.org/10.1016/0040-1951(94)00184-B).
- 840 Petzold, A. & Hinz, W. 1976. *Silikatchemie*. Leipzig, VEB.
- 841 Poliakov, A.N.B., Dmowska, R. & Rice, J.R. 2002. Dynamic shear rupture interactions with fault bends  
842 and off-axis secondary faulting. *Journal of Geophysical Research: Solid Earth*, **107**, 2295,  
843 <https://doi.org/10.1029/2001JB000572>.
- 844 Pollard, D.D. & Aydin, A. 1984. Propagation and linkage of oceanic ridge segments. *Journal of*  
845 *Geophysical Research: Solid Earth*, **89**, 10017–10028,  
846 <https://doi.org/10.1029/JB089iB12p10017>.
- 847 Pollard, D.D., Segall, P. & Delaney, P.T. 1982. Formation and interpretation of dilatant echelon  
848 cracks. *Geological Society of America Bulletin*, **93**, 1291–1303, [https://doi.org/10.1130/0016-7606\(1982\)93<1291:FAIODE>2.0.CO;2](https://doi.org/10.1130/0016-7606(1982)93<1291:FAIODE>2.0.CO;2).
- 850 Price, N.A., Johnson, S.E., Gerbi, C.C. & West, D.P. 2012. Identifying deformed pseudotachylite and  
851 its influence on the strength and evolution of a crustal shear zone at the base of the  
852 seismogenic zone. *Tectonophysics*, **518–521**, 63–83,

- 853 <https://doi.org/10.1016/j.tecto.2011.11.011>.
- 854 Rainbird, R. H., Hamilton, M. A., & Young, G. M. (2001). Detrital zircon geochronology and  
855 provenance of the Torridonian, NW Scotland. *Journal of the Geological Society*, **158**(1), 15–27.  
856 <https://doi.org/10.1144/jgs.158.1.15>
- 857 Robie, R.A., Hemingway, B.S. & Fisher, J.R. 1979. *Thermodynamic Properties of Minerals and Related*  
858 *Substances at 298.15 K and 1 Bar ( 105 Pascals) Pressure and at Higher Temperatures*.  
859 Washington.
- 860 Rowe, C.D. & Griffith, W.A. 2015. Do faults preserve a record of seismic slip: A second opinion.  
861 *Journal of Structural Geology*, **78**, 1–26,  
862 <https://doi.org/http://dx.doi.org/10.1016/j.jsg.2015.06.006>.
- 863 Rowe, C.D., Moore, J.C., Meneghini, F. & McKeirnan, A.W. 2005. Large-scale pseudotachylites and  
864 fluidized cataclasites from an ancient subduction thrust fault. *Geology*, **33**, 937–940,  
865 <https://doi.org/10.1130/g21856.1>.
- 866 Rowe, C.D., Meneghini, F. & Moore, J.C. 2011. Textural record of the seismic cycle: strain-rate  
867 variation in an ancient subduction thrust. *Geological Society, London, Special Publications*, **359**,  
868 77–95, <https://doi.org/10.1144/sp359.5>.
- 869 Rowe, C.D., Kirkpatrick, J.D. & Brodsky, E.E. 2012. Fault rock injections record paleo-earthquakes.  
870 *Earth and Planetary Science Letters*, **335–336**, 154–166,  
871 <https://doi.org/10.1016/j.epsl.2012.04.015>.
- 872 Rowe, C.D., Ross, C., et al. 2018. Geometric Complexity of Earthquake Rupture Surfaces Preserved in  
873 Pseudotachylite Networks. *Journal of Geophysical Research: Solid Earth*, **123**, 7998–8015,  
874 <https://doi.org/10.1029/2018JB016192>.
- 875 Ruppert, N.A., Rollins, C., Zhang, A., Meng, L., Holtkamp, S.G., West, M.E. & Freymueller, J.T. 2018.  
876 Complex Faulting and Triggered Rupture During the 2018 MW 7.9 Offshore Kodiak, Alaska,  
877 Earthquake. *Geophysical Research Letters*, **45**, 7533–7541,  
878 <https://doi.org/10.1029/2018GL078931>.
- 879 Sawyer, W.J. & Resor, P.G. 2017. Modeling frictional melt injection to constrain coseismic physical  
880 conditions. *Earth and Planetary Science Letters*, **469**, 53–63,  
881 <https://doi.org/https://doi.org/10.1016/j.epsl.2017.04.012>.
- 882 Segall, P. & Pollard, D.D. 1983. Nucleation and growth of strike slip faults in granite. *Journal of*  
883 *Geophysical Research: Solid Earth*, **88**, 555–568, <https://doi.org/10.1029/JB088iB01p00555>.
- 884 Sherlock, S.C., Jones, K.A. & Park, R.G. 2008. Grenville-age pseudotachylite in the Lewisian:  
885 laserprobe  $^{40}\text{Ar}/^{39}\text{Ar}$  ages from the Gairloch region of Scotland (UK). *Journal of the Geological*  
886 *Society*, **165**, 73–83, <https://doi.org/10.1144/0016-76492006-134>.
- 887 Sibson, R. 1986. Brecciation processes in fault zones: Inferences from earthquake rupturing. *Pure*  
888 *and Applied Geophysics*, **124**, 159–175, <https://doi.org/10.1007/bf00875724>.
- 889 Sibson, R.H. 1975. Generation of pseudotachylite by ancient seismic faulting. *Geophysical Journal*  
890 *of the Royal Astronomical Society*, **43**, 775, [https://doi.org/10.1111/j.1365-](https://doi.org/10.1111/j.1365-246X.1975.tb06195.x)  
891 [246X.1975.tb06195.x](https://doi.org/10.1111/j.1365-246X.1975.tb06195.x).
- 892 Sibson, R.H. 1985. Stopping of earthquake ruptures at dilational fault jogs. *Nature*, **316**, 248.
- 893 Spray, J.G. 2010. Frictional Melting Processes in Planetary Materials: From Hypervelocity Impact to  
894 Earthquakes Jeanloz, R. & Freeman, K. H. (eds). *Annual Review of Earth and Planetary Sciences*,

- 895           **38**, 221–254, <https://doi.org/10.1146/annurev.earth.031208.100045>.
- 896   Stewart, A. D. (2002). *The later Proterozoic Torridonian rocks of Scotland; their sedimentology,*  
897       *geochemistry and origin*. Bath: Geological Society of London.
- 898   Streule, M. J., Strachan, R. A., Searle, M. P., & Law, R. D. (2010). Comparing Tibet-Himalayan and  
899       Caledonian crustal architecture, evolution and mountain building processes. *Geological Society,*  
900       *London, Special Publications*, **335**(1), 207–232. <https://doi.org/10.1144/sp335.10>
- 901   Swanson, M.T. 1988. Pseudotachylyte-bearing strike-slip duplex structures in the Fort Foster Brittle  
902       Zone, S. Maine. *Journal of Structural Geology*, **10**, 813–828,  
903       [https://doi.org/http://dx.doi.org/10.1016/0191-8141\(88\)90097-1](https://doi.org/http://dx.doi.org/10.1016/0191-8141(88)90097-1).
- 904   Swanson, M.T. 1989. Sidewall ripouts in strike-slip faults. *Journal of Structural Geology*, **11**, 933–948,  
905       [https://doi.org/https://doi.org/10.1016/0191-8141\(89\)90045-X](https://doi.org/https://doi.org/10.1016/0191-8141(89)90045-X).
- 906   Swanson, M.T. 1992. Fault structure, wear mechanisms and rupture processes in pseudotachylyte  
907       generation. *Tectonophysics*, **204**, 223–242, [https://doi.org/10.1016/0040-1951\(92\)90309-T](https://doi.org/10.1016/0040-1951(92)90309-T).
- 908   Swanson, M.T. 2005. Geometry and kinematics of adhesive wear in brittle strike-slip fault zones.  
909       *Journal of Structural Geology*, **27**, 871–887, <https://doi.org/10.1016/j.jsg.2004.11.009>.
- 910   Tchalenko, J.S. & Berberian, M. 1975. Dasht-e Ba'az Fault, Iran: Earthquake and Earlier Related  
911       Structures in Bed Rock. *GSA Bulletin*, **86**, 703–709.
- 912   Techmer, K.S., Ahrendt, H. & Weber, K. 1992. The development of pseudotachylyte in the Ivrea—  
913       Verbano Zone of the Italian Alps. *Tectonophysics*, **204**, 307–322,  
914       [https://doi.org/https://doi.org/10.1016/0040-1951\(92\)90314-V](https://doi.org/https://doi.org/10.1016/0040-1951(92)90314-V).
- 915   Toy, V.G., Ritchie, S. & Sibson, R.H. 2011. Diverse habitats of pseudotachylytes in the Alpine Fault  
916       Zone and relationships to current seismicity Fagereng, A., Toy, V. G. & Rowland, J. V (eds).  
917       *Geological Society, London, Special Publications*, **359**, 115–133,  
918       <https://doi.org/10.1144/sp359.7>.
- 919   Turnbull, M. J. M., Whitehouse, M. J., & Moorbath, S. (1996). New isotopic age determinations for  
920       the Torridonian, NW Scotland. *Journal of the Geological Society*, **153**(6), 955–964.
- 921   Ujiié, K., Yamaguchi, H., Sakaguchi, A. & Toh, S. 2007. Pseudotachylytes in an ancient accretionary  
922       complex and implications for melt lubrication during subduction zone earthquakes. *Journal of*  
923       *Structural Geology*, **29**, 599–613, <https://doi.org/http://dx.doi.org/10.1016/j.jsg.2006.10.012>.
- 924   Wang, H., Li, H., Janssen, C., Sun, Z. & Si, J. 2015. Multiple generations of pseudotachylyte in the  
925       Wenchuan fault zone and their implications for coseismic weakening. *Journal of Structural*  
926       *Geology*, **74**, 159–171, <https://doi.org/http://dx.doi.org/10.1016/j.jsg.2015.03.007>.
- 927   Whitehouse, M.J., Bridgwater, D. & Park, R.G. 1997. Detrital zircon ages from the Loch Maree Group,  
928       Lewisian Complex, NW Scotland: confirmation of a Palaeoproterozoic Laurentia—Fennoscandia  
929       connection. *Terra Nova*, **9**, 260–263, <https://doi.org/10.1111/j.1365-3121.1997.tb00025.x>.
- 930
- 931

Parameter	Description	Value	Source
$\rho$	density	2809 kg m <sup>-3</sup>	[a]
w	pseudotachylyte width	0.005 m	See Fig. 7a
$\tau$	shear stress on fault	107-155 MPa	
$\phi$	ratio of clasts to crystalline matrix	0.11	
H	latent heat of melting	135213 J kg <sup>-1</sup>	[a]
C <sub>p</sub>	specific heat	1017 J kg <sup>-1</sup> K <sup>-1</sup>	[a]
T <sub>melt</sub>	coseismic melt temperature	1023 - 1623 K	[b]
T <sub>ambient</sub>	ambient host rock temperature	518-618 K	[c]
G	shear modulus	49 GPa	[d]

933 **Table 1:** Thermal and mechanical properties attributed to the GSZ amphibolite and the  
934 pseudotachylyte faults within them. Obtained from [a] values for tremolite, anorthite and quartz in  
935 Robie et al. (1979); [b] melting temperatures for hornblende and oligoclase in Spray (2010); [c]  
936 geothermal gradient of 25°C km<sup>-1</sup>, modified from Droop et al. (1999); [d] values for hornblende,  
937 anorthite and quartz presented in Hacker et al. (2003) and originally sourced from Ohno (1995) and  
938 Holland & Powell (2004).

939

940 **Figure captions**

941 **Figure 1.** Pseudotachylyte in the Gairloch Shear Zone: **(a)** Location of the Gairloch Shear Zone and  
942 simplified lithological map (modified from Lei & Park 1993) showing localities where  
943 pseudotachylytes are found within amphibolites; **(b)** typical yellow-grey weathered pseudotachylyte  
944 within foliated amphibolite - the pseudotachylyte veins here includes the generating fault vein  
945 (indicated by white arrowheads) plus injection veins protruding at a high angle from the fault  
946 [57.7122°N 05.6240°W]; **(c)** typical grey fresh surface of pseudotachylyte, two overlapping  
947 pseudotachylyte veins within darker amphibolite [57.7066°N 05.6173°W].

948 **Figure 2.** Idealised types of pseudotachylyte (PST) fault vein geometries observed in the Gairloch  
949 Shear Zone amphibolites: **(a)** idealised single linear pseudotachylyte (PST) fault vein with typical  
950 geometry of injection veins protruding into the host rock; **(b)** Segmented fault composed of several  
951 parallel pseudotachylyte fault veins that may be linked across the stepover section, either by one  
952 segment tip or by the tips of both segments. The pseudotachylyte vein is continuous across the

953 linkage; **(c)** Segmented fault composed of several parallel pseudotachylyte fault veins, with  
954 extensional rhombocasm pull-aparts identifiable in the stepover. The pseudotachylyte vein is  
955 continuous across the stepover; **(d)** Parallel and closely-spaced pseudotachylyte fault veins bounding  
956 a region with internal vein networks – at least some of which are fault veins – and possibly  
957 brecciation, in which case a tabular breccia is formed; **(e)** Pseudotachylyte fault vein which splits into  
958 two branches, which may display different vein thicknesses. Both branches should have  
959 accommodated shear displacement and PST injection veins or brecciation may be associated with  
960 the branches.

961 **Figure 3.** Typical microscopic features of GSZ pseudotachylytes: **(a)** optical micrograph of branching  
962 pseudotachylyte vein with high angle injection and side-wall shortcut removing curve in the vein  
963 (plane polarised light) sampled from [57.7008°N 05.6308°W]; **(b)** optical micrograph of  
964 pseudotachylyte matrix illustrating banded variation in crystal morphology (plane polarised light)  
965 sampled from [57.7066°N 05.6173°W]; **(c)** back scattered electron image of pseudotachylyte  
966 crystalline matrix capturing heterogeneous hornblende nucleation around a plagioclase clast,  
967 sampled from [57.7066°N 05.6173°W]; **(d)** back scattered electron image of pseudotachylyte matrix  
968 with radiating dendritic and microlitic hornblende, sampled from [57.7066°N 05.6173°W]; **(e)** optical  
969 micrograph of deformed hornblende clasts in pseudotachylyte (plane polarised light), sampled from  
970 [57.7008°N 05.6308°W]; **(f)** optical micrograph of deformed hornblende in intersection of injection  
971 and fault veins (plane polarised light), sampled from [57.7008°N 05.6308°W].

972 **Figure 4.** Stepped pseudotachylyte fault vein following amphibolite foliation [57.6959°N 05.6161°W];  
973 **(a)** In the field, the fault vein (emphasised by orange shading) shows lateral steps (one indicated by  
974 arrowhead). The pseudotachylyte thickness along the fault varies from 3 - 15 mm, hammer length is  
975 30 cm. Image shows a horizontal surface. An unannotated version of this image is available as  
976 Supplementary Figure 1; **(b)** fresh cut surface of grey pseudotachylyte fault veins with chilled  
977 margins sampled from the locality shown in Fig. 4a. White box shows location of Fig. 4c; **(c)** optical

978 micrograph of a stepover section with one overstep linked by only one segment (far right) and one  
979 preserved in the process of linkage involving both fault segment tips (centre) which curve towards  
980 the adjacent segment. A band of cataclasite, indicated by white arrowheads, is parallel to and  
981 partially overprinted by a pseudotachylyte segment (plane polarised light); **(d)** and **(e)** micrographs  
982 showing detail of ductile shear zones propagating in front of fault tips forming a process zone (plane  
983 polarised light).

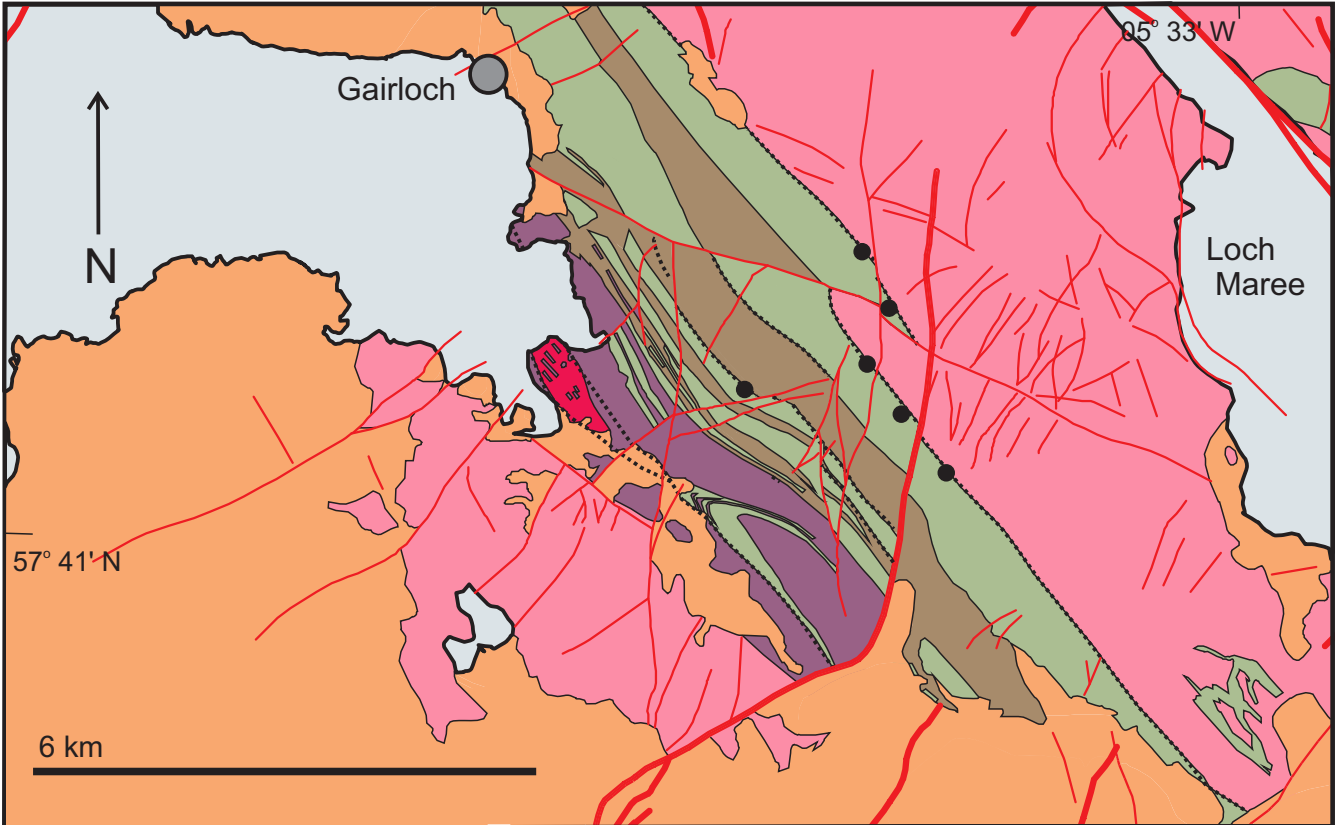
984 **Figure 5.** Field-scale geometries of pseudotachylyte (PST) faults in GSZ amphibolites. All photos have  
985 PST traced in orange – unannotated versions are available in supplementary figure 2: **(a)** pull-apart  
986 rhombochasm forms dilational stepover within pseudotachylyte fault cutting quartz vein in  
987 amphibolite (pencil length 15 cm) [57.7007°N 05.6173°W]; **(b)** reactivation of pre-existing shear  
988 band, with pseudotachylyte lining boundary (white lines) and internal (blue lines) faults as well as  
989 injecting into foliation and locally developing into pseudotachylyte breccias. Horizontal plane of  
990 exposure [57.7121°N 05.6228°W]; **(c)** reactivation of shear bands by brittle, pseudotachylyte-bearing  
991 faults, with breccia extensively developed in the underlying band. Horizontal plane of exposure  
992 [57.7668°N 05.6168°W]; **(d)** large pseudotachylyte fault branching at its tip. Vertical plane of  
993 exposure [57.7007°N 05.6304°W]; **(e)** branching pseudotachylyte fault with injection veins  
994 developed off the thicker branch. Horizontal plane of exposure [57.6904°N 05.6066°W]; **(f)** angular,  
995 wedge-shaped breccia developed between two non-parallel faults, potentially part of a paired fault  
996 zone. Horizontal plane of exposure [57.7070°N 05.6219°W].

997 **Figure 6.** Microscale geometries of pseudotachylyte veins in optical micrographs: **(a)** millimetre scale  
998 steps in pseudotachylyte vein margin (plane polarised light) sampled from [57.7695°N 05.6132°W];  
999 **(b)** millimetre scale steps in vein margin with additional grain-scale roughness indicated by  
1000 arrowheads (plane polarised light) sampled from [57.7066°N 05.6173°W]; **(c)** ragged edge of  
1001 polycrystalline clast indicates partial melting (plane polarised light) sampled from [57.7695°N  
1002 05.6132°W]; **(d)** partially melted polycrystalline clast with amphibole replaced by pseudotachylyte

1003 and quartz and plagioclase preserved (cross polarised light) sampled from [57.7066°N 05.6173°W];  
1004 **(e)** short and blunt-ended injection veins (cross-polarised light) sampled from [57.7007°N  
1005 05.6304°W]; **(f)** blunt-ended injection vein with thin extensions (plane polarised light) sampled from  
1006 [57.7008°N 05.6308°W]; **(g)** margin of pseudotachylyte vein where sidewall shortcut feature has  
1007 straightened margin by removing a step. New clasts are already rounded and rotated (plane  
1008 polarised light), sampled from [57.7066°N 05.6173°W].

1009 **Figure 7.** Estimation of shear stress and coseismic temperature change on GSZ seismic faults; **(a)**  
1010 Mohr circle construction for lithostatic stress state and strike-slip fault regime; **(b)** range of minimum  
1011 seismic displacement necessary to produce thickness of 5 mm pseudotachylyte along a fault slipping  
1012 at different depths in the crust. Equivalent moment magnitudes ( $M_w$ ) are indicated for faults with  
1013 the maximum and minimum estimated lengths of 100 m and 1 m respectively.

1014 **Figure 8.** Models of formation of stepping ruptures and dilational sites through a single episode of  
1015 seismic slip; **(a)** linkage of pseudotachylyte-bearing rupture segments in the 'dilational crack' style;  
1016 **(b)** linkage of rupture segments via secondary faults forming dilatational pull-aparts in extensional  
1017 stepovers; **(c)** Formation of elongate tabular breccias via paired ruptures and internal faults, here  
1018 exploiting a shear band structure.



**Neoproterozoic sediments**

 Torridon Group


**Palaeoproterozoic supracrustals (Loch Maree Group)**


 Metasedimentary rocks, predominantly metapelite

 Amphibolite

 Reworked granodiorite-tonalite gneiss

**Archean gneiss**

 Hornblende gneiss

 Undifferentiated Lewisian orthogneiss (with amphibolite dykes)

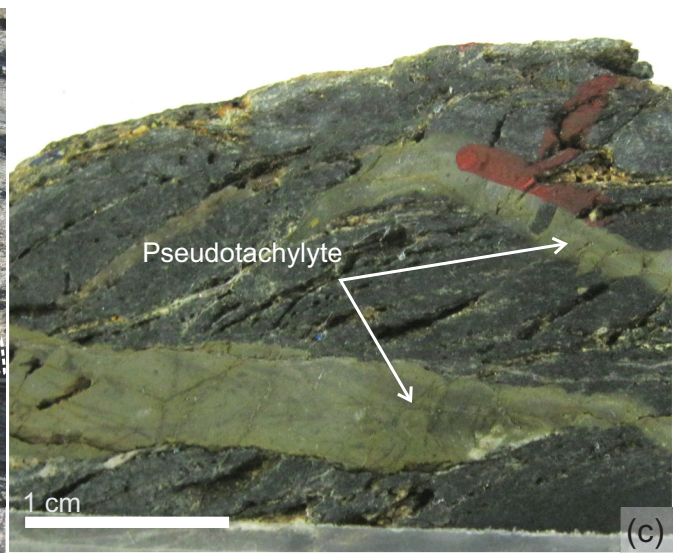
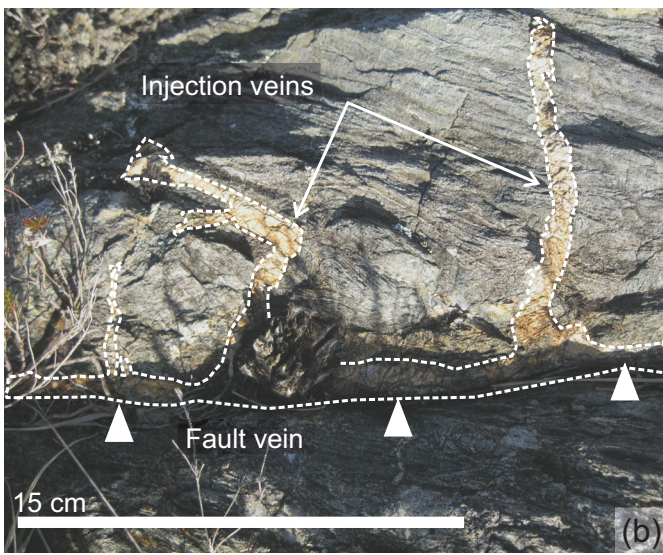
 Crush Belt (after Park, 1961)

 Pseudotachylite in amphibolite

 Large fault

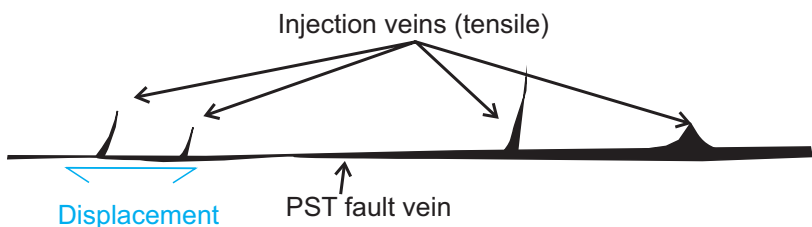
 Local faults

(a)

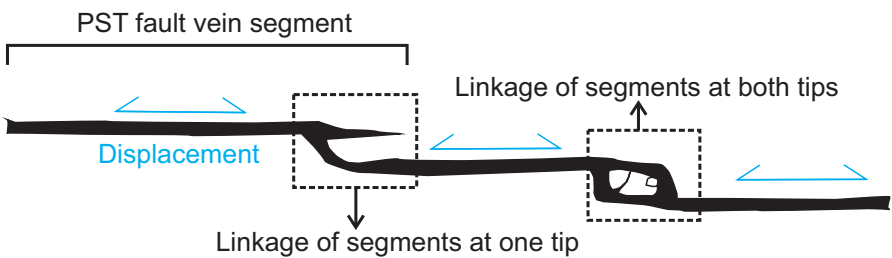




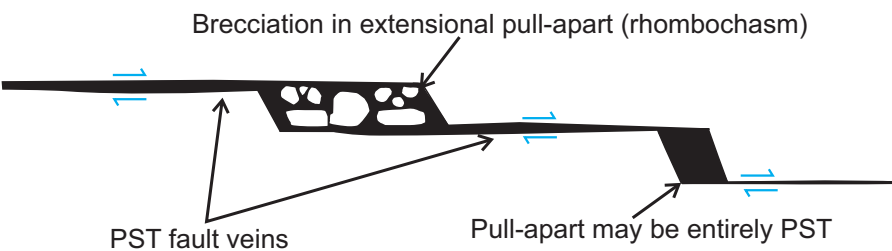
(a) Single fault vein with injection veins



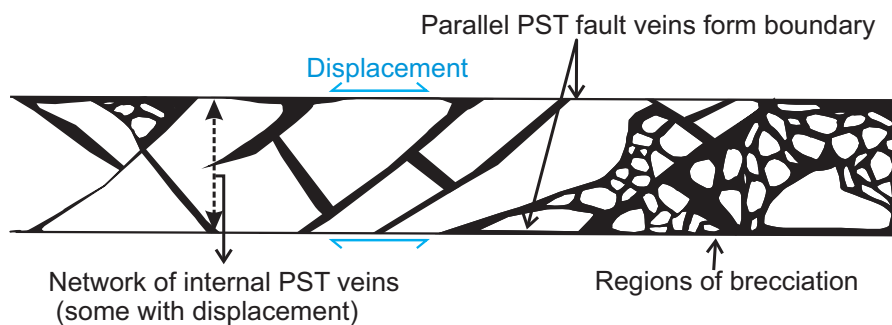
(b) Segmented fault veins with linkage



(c) Segmented fault veins with pull-aparts



(d) Paired fault veins with internal PST networks



(e) Branching fault vein

